Lukas Elsinger, BSc

Sub-wavelength grating lens designs for wafer-level IR optics

MASTER'S THESIS

to achieve the university degree of

Diplom-Ingenieur

Master's degree programme: Technical Physics

submitted to

Graz University of Technology

Supervisor

Univ.-Prof. Ph. D. Peter Hadley

Institute of Solid State Physics

in cooperation with ams AG

Graz, September 2015

AFFIDAVIT

I declare that I have authored this thesis independently, that I have not used other than the declared sources/resources, and that I have explicitly indicated all material which has been quoted either literally or by content from the sources used. The text document uploaded to TUGRAZonline is identical to the present master‘s thesis dissertation.

Date

Signature

Abstract

Flat transmissive lenses can reduce the size and cost of micro-optical devices. For wafer-level infrared applications, standard lithographic techniques may be used for the production.

Lenses based on sub-wavelength gratings were designed using a finite difference time domain program (Lumerical). It was observed, that the grating structures also support undesirable lateral modes. Despite the sub-wavelength geometry of the structure, the onset of scattering into higher diffraction orders could be accurately described by Fraunhofer far field diffraction theory. It was shown by wave-optics simulations, that sub-wavelength grating lenses can be optimized for imaging with a 120° field of view. This main result of the work was presented at the 2015 SPIE Optics + Photonics conference [1]. The chromatic aberrations of lenses designed for wavelengths of 4 μm and 10 μm were also analyzed using a finite element method program (Comsol) and found to match theoretical predictions. A sensitivity analysis of the lens performance with respect to deviations from the ideal geometry showed the feasibility of production.

Test samples for a wavelength of 10 μm were produced using UV lithography and characterized using a scanning slit measurement set-up with a broadband thermal IR source. Simulation and measurement results were compared, showing good agreement of the width of the focal spot. Generally it was found that lenses with a low numerical aperture show better focusing efficiency than high NA lenses. This was attributed to under-sampling of the phase profile by the grating pitch near the lens boundary.

Contents

1 INTRODUCTION

Micro-optical elements are key parts of many products and applications today. In the ongoing miniaturization of devices, wafer-level optics and wafer-level integration are an established way to reduce size and cost [2]. Figure 1.1 illustrates these technologies. Wafer-level optics implies that many of the sketched Fresnel lenses are produced in parallel on a single wafer, using for instance nano-imprint lithography to create the structures [2]. For wafer-level integration, the optics wafer is bonded directly to the wafer with the sensor elements. Using such a technology can significantly reduce the cost for the assembly of the devices.

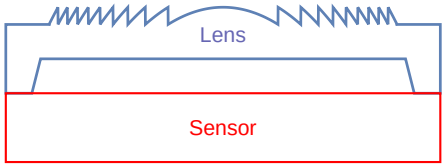

Figure 1.1: Wafer-level optics and wafer-level integration are key technologies for micro-optical elements, reducing size and cost [2].

Besides Fresnel lenses, also conventional refractive lenses and diffractive optical elements are currently used for micro-optical devices [3]. In further advancing the miniaturization, there are other promising concepts for thin flat lenses based on dielectric gratings [4, 5] and plasmonic nano-antennas [6] with extremely compact geometry. Similar to established diffractive optical elements [7], those lenses can be thought of as a layer, that reshapes the incident wavefront.

The idea of using sub-wavelength features etched into dielectrics in order to achieve an arbitrary change of the transmitted phase dates back more than 20 years [8]. Initially, the designs were based on an effective medium theory [9]. The assumption is, that if the features are sufficiently small, compared to the wavelength, the material behaves like a medium with an effective refractive index. This can be used to locally vary the optical distance and thereby the transmitted phase, which allows for the construction of a lens.

More recently, sub-wavelength gratings with a pitch too large to be accurately described by effective medium theory, but still much smaller than for conventional diffraction gratings, have gained increased interest [10]. For these structures, with a ratio of grating pitch Λ to wavelength λ of around one, the full behavior can only be described by rigorous diffraction theory. Figure 1.2 compares the methods used to describe gratings with different pitch. For conventional diffractive optical elements Λ/λ is usually larger than 10, so the complex transmittance amplitude method can be used to design their functionality [7].

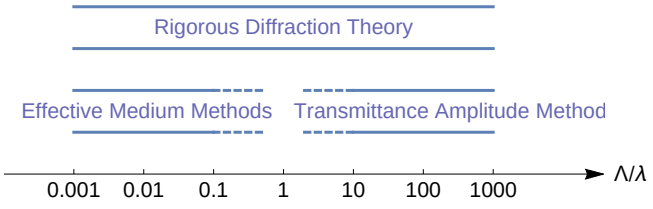

Figure 1.2: Methods used for the description of grating structures depend on ratio of grating pitch Λ to wavelength λ [7]. The full behavior of sub-wavelength gratings with $\Lambda/\lambda \sim 1$ can only be described by rigorous diffraction theory.

Sub-wavelength gratings can show extraordinary properties such as broadband high reflec-

tion and transmission, caused by the high sensitivity of the light interaction to the local geometry of the grating [10]. Among many other applications, e.g. tunable top reflectors for vertical cavity surface emitting lasers (VCSEL) [10], focusing ability has been shown, both for reflective [11] and for transmissive designs [4, 5].

Compared to lenses, that use a plasmonic nano-antenna array [6] to change the transmitted phase, sub-wavelength grating lens designs have been reported to achieve significantly higher focusing efficiency above 80% [5]. In addition, for the IR range, sufficiently accurate production of sub-wavelength structures is possible with standard UV lithography [4]. This makes sub-wavelength grating lenses an interesting candidate for wafer-level IR optics.

2 FLAT TRANSMISSIVE LENS DESIGN

In order to build any flat transmissive lens, it is necessary to know, how the incident wavefront has to be reshaped to produce a focal spot at a distance f. This means, that one has to find a function for the transmitted phase $\phi(r, f)$ at a radius r.

2.1 Huygens-Fresnel principle

For the simplest geometry, where the thin lens is placed on top of the substrate and the focal length f is less than the substrate thickness, the phase function can be found using only the Huygens-Fresnel principle [12]. This basic principle of optics states, that each point of a wavefront can be seen as the source of a spherical wave. In order for a focal spot to occur at point F, the waves from each point P have to be in phase. The phase function $\phi(r)$ of the flat lens therefore has to compensate for the difference in optical path length.

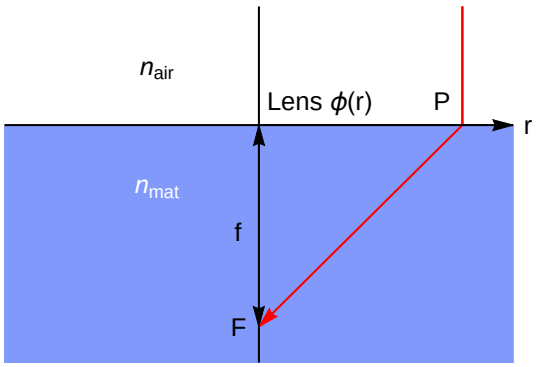

Figure 2.1: For this geometry the Huygens-Fresnel principle was used to find the phase $\phi(r)$ at radius r for a focal length f of the flat transmissive lens.

This means that the phase ϕ at radius r for a lens with focal length f and propagation in a material with refractive index n_{mat} has to be

$$\phi(r, f) = \frac{2\pi}{\lambda} n_{mat} \left(f - \sqrt{f^2 + r^2} \right). \tag{2.1}$$

Because adding a multiple of 2π to the phase does not change the fields, a modified phase function of

$$\tilde{\phi} = \phi \mod 2\pi m, \qquad m \in \mathbb{N} \tag{2.2}$$

can be used as well. For $m = 1$ it is sufficient to be able to vary the transmitted phase in the lens plane from 0 to 2π.

2.2 Fermat's principle

In many cases the simple geometry presented above is not applicable and one wants to have the focal spot on the opposite side of the substrate. Equation 2.1 therefore has to be modified, because it doesn't account for the light being refracted at the additional interface. To solve this issue, Fermat's principle [12] can be used. In one formulation this principle states, that optical path length S is stationary. Applied to the geometry in Figure 2.2 the optical path length is

$$S = \int_P^F n \, \mathrm{d}s. \tag{2.3}$$

And the stationarity condition is written as

$$\delta S = \delta \int_P^F n \, \mathrm{d}s = 0. \tag{2.4}$$

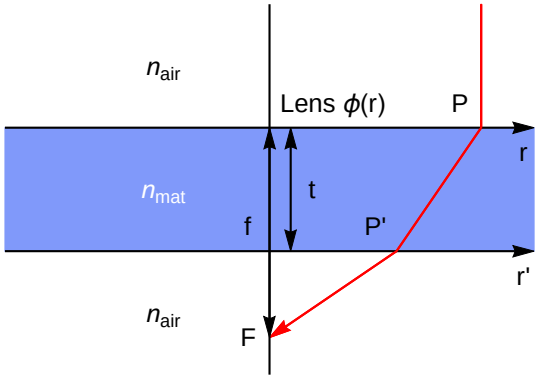

Figure 2.2: The derivation of the phase function $\phi(r)$ for a thin flat lens with an additional interface at the back side of the wafer can be done using Fermat's principle.

Considering straight line dispersion of light in media with an isotropic and constant refractive index, the length of the optical path is

$$S(r, r', f, t) = \sqrt{(f-t)^2 + r'^2} + n_{mat}\sqrt{t^2 + (r-r')^2}. \tag{2.5}$$

The stationarity condition then can be rewritten as

$$\left|\frac{\partial S}{\partial r'}\right|_{r'=r'_{stat}} = \frac{r'}{\sqrt{(f-t)^2 + r'^2}} - \frac{n_{mat}(r-r')}{\sqrt{t^2 + (r-r')^2}} = 0, \tag{2.6}$$

which can be solved numerically for r'_{stat}. By putting the obtained value into Equation 2.5 and again using the Huygens-Fresnel principle one can find the desired phase function. However, it turned out from full wave-optics simulations, that the geometrical optics considerations used in this derivation did not give the desired focal length f for the simulated geometries. Therefore the empirical correction

$$r'_{emp} = \frac{1}{3}\left(r'_{stat} + 2\frac{f-t}{r}\right) \tag{2.7}$$

was used to find a more suitable phase function for the simulated geometries

$$\phi(r, f, t) = \frac{2\pi}{\lambda}\left(f + t \cdot (n_{mat} - 1) - S(r, r'_{emp}, f, t)\right). \tag{2.8}$$

3 EFFECTIVE MEDIUM THEORY

First, an effective medium theory was used to design a thin flat lens with a gradient index. Wave-optics simulations of the lens showed reasonable focusing performance of the lens, but the main disadvantage of the lens design was the rather large aspect ratio of approximately 1:11 for the structures.

3.1 Effective index of a one-dimensional grating

For gratings with a sufficiently small ratio of pitch Λ to wavelength λ, it is possible to describe the propagation of electromagnetic waves by means of an effective medium theory [9]. A structure consisting of two isotropic materials with different properties, is approximated by an anisotropic effective medium. For the example of a one-dimensional periodic structure, consisting of layers with a refractive index n_1 and n_2, the effective index of refraction is different for different propagation directions and polarizations. Rytov [9] gives a derivation of the effective refractive index of a one-dimensional grating to second order in Λ/λ. For propagation in the direction of the layers, illustrated in Figure 3.1, there is a different refractive index for TE and TM polarized incidence.

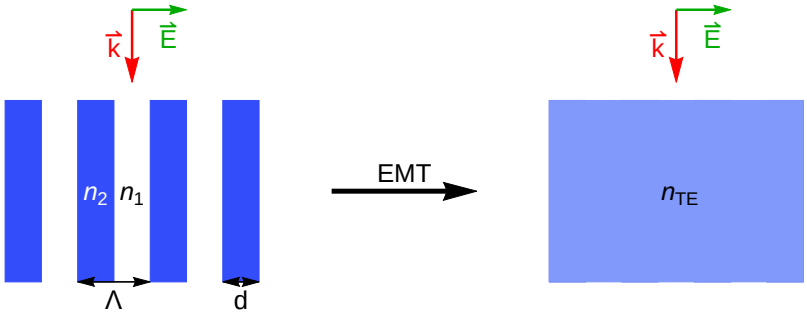

Figure 3.1: Effective medium theory for a one-dimensional grating and propagation in direction of the layers. The material consists of layers with refractive index n_1 and n_2, alternating with pitch Λ. The layers with refractive index n_2 have a thickness d. For TE polarized incidence, the grating structure is approximated by an effective medium with refractive index n_{TE}.

The zero-order effective refractive index of a grating structure, made from non-magnetic materials, for TM polarized incidence is

$$n_{0TM}^2 = \left(1 - \frac{d}{\Lambda}\right) n_1^2 + \frac{d}{\Lambda} n_2^2. \tag{3.1}$$

In this notation Λ is the grating pitch and d is the thickness of the layers with refractive index n_2. For TE polarized incidence, the zero-order effective refractive index is

$$n_{0TE}^{-2} = \left(1 - \frac{d}{\Lambda}\right) n_1^{-2} + \frac{d}{\Lambda} n_2^{-2}. \tag{3.2}$$

For the case of a grating, consisting of silicon pillars and air, zero order effective medium theory fails for $\Lambda/\lambda \geq 0.1$ [13]. A second-order correction [9] makes it possible to extend the validity of the effective medium approach to some extent. For TM polarized incidence, the effective refractive index to second order in Λ/λ for a one-dimensional grating is

$$n_{TM}^2 = n_{0TM}^2 \left[1 + \frac{\pi^2}{3} \left(\frac{\Lambda}{\lambda}\right)^2 \left(\frac{d}{\Lambda}\right)^2 \left(1 - \frac{d}{\Lambda}\right)^2 \left(n_2^2 - n_1^2\right)^2\right]. \tag{3.3}$$

For the TE polarization, the effective refractive index to second order in Λ/λ is

$$n_{TE}^2 = n_{0TE}^2 \left[1 + \frac{\pi^2}{3} \left(\frac{\Lambda}{\lambda} \right)^2 \left(\frac{d}{\Lambda} \right)^2 \left(1 - \frac{d}{\Lambda} \right)^2 \left(n_2^2 - n_1^2 \right)^2 n_{0TM}^2 \left(\frac{n_{0TE}^2}{n_1^2 n_2^2} \right)^2 \right]. \tag{3.4}$$

3.2 Effective index of a two-dimensional grating

To find the effective refractive index of a two-dimensional grating, the grating should be considered as a photonic crystal [14]. By calculating the photonic dispersion relation and then looking at the limit as $k \to 0$, a value for the effective refractive index n_{2D} can be obtained.

Another approach to find an effective refractive index for two-dimensional gratings can be found in Reference [13]. Rather than calculating the dispersion relation of a two-dimensional structure, the effective index is approximated as the average of the effective indexes of two one-dimensional structures. Figure 3.2 illustrates a symmetric structure made of materials with index n_1 and n_2, which is approximated by an effective medium, with the same effective index n_{2D} for TE and TM polarized incidence.

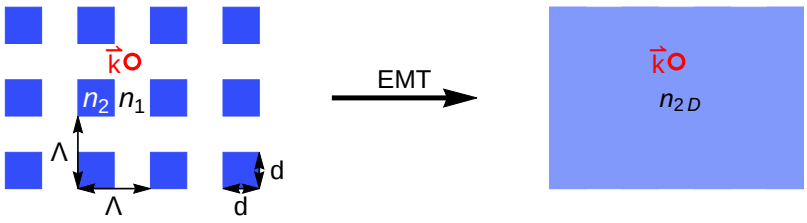

Figure 3.2: Effective medium theory for a two-dimensional grating with incidence normal to the grating plane. The grating consists of two materials with refractive index n_1 and n_2. The pitch Λ and the with d of the material with index n_2 is the same in both directions. Symmetry demands, that the effective refractive index n_{2D} is the same for the TE and the TM polarization.

In Reference [13], the two-dimensional structure is considered to behave as the average of two one-dimensional structures. For the first one-dimensional structure, the incident light is TM polarized. The respective zero-order effective refractive index is $\hat{n}_{2D}$. For the second structure, the light is TE polarized. This gives an effective index $\check{n}_{2D}$ for the second one-dimensional structure. The resulting formula for the effective refractive index of a two-dimensional grating is

$$n_{2D} = \frac{\hat{n}_{2D} + \check{n}_{2D}}{2}. \tag{3.5}$$

Zero-order effective medium theory is used to find the effective index of the one-dimensional sub-structures to be

$$\hat{n}_{2D}^2 = \left(1 - \frac{d}{\Lambda} \right) n_1^2 + \frac{d}{\Lambda} n_{TE}^2 \qquad \text{and} \tag{3.6}$$

$$\check{n}_{2D}^{-2} = \left(1 - \frac{d}{\Lambda} \right) n_1^{-2} + \frac{d}{\Lambda} n_{TM}^{-2}. \tag{3.7}$$

3.3 EMT lens design for a wavelength of 10 μm

For a design wavelength of $\lambda = 10$ μm, silicon with a refractive index of $n_{Si} = 3.4215$ [15] and air can be used for the grating. The first possibility is to have silicon pillars with

$n_2 = n_{Si}$ and $n_1 = 1$. But it is also possible to etch holes into silicon, corresponding to a notation of $n_1 = n_{Si}$ and $n_2 = 1$ in the above formulas and in Figure 3.2.
Figure 3.3 shows the effective refractive index of a two-dimensional grating structure, calculated for silicon pillars and holes in silicon from Equation 3.5. In this particular implementation, a pitch of $\Lambda = 2.4$ μm was used. For this choice, corresponding to $\Lambda/\lambda = 0.24$, second-order effective medium theory is still valid [13]. For the production of a grating structure, it is necessary to limit the width d of the grating pillars and the hole diameter. Restricting d gives a maximum value for the achievable difference of the effective refractive index Δn_{max}.

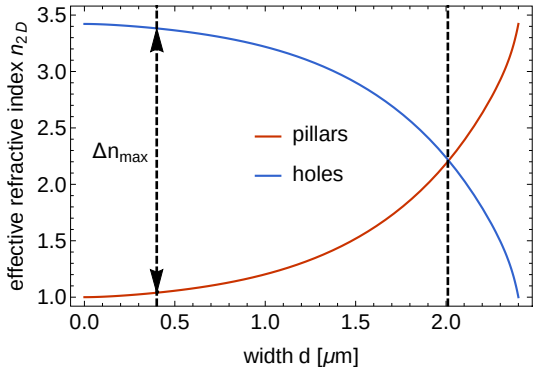

Figure 3.3: Effective refractive index of a two-dimensional grating calculated from Equation 3.5. Silicon pillars correspond to $n_2 = n_{Si}$ and $n_1 = 1$. Holes correspond to $n_1 = n_{Si}$ and $n_2 = 1$. For both, a pitch of $\Lambda = 2.4$ μm was used. Restricting the width d gives a maximum value for the achievable difference of the effective refractive index Δn_{max}.

The difference of the refractive index Δn refers to the notation

$$n_{2D}(r) = n_{min} + \Delta n(r), \tag{3.8}$$

that was used to find the effective refractive index $n_{2D}(r)$ at radius r for a flat transmissive lens with a focal length f. For this particular design, the minimum refractive index n_{min} was

$$n_{min} = n_{2D}(n_1 = 1, n_2 = n_{Si}, d = 0.4\,\mu\text{m}) \tag{3.9}$$

Figure 3.4 shows the schematics of a transmissive flat lens design based on effective medium theory. A plane wave with wave vector $\vec{k}$ is focused by a two-dimensional grating structure with an effective refractive index $n_{2D}(r)$ at radius r. In the used design, the pillars and holes had constant pitch Λ and height h, while the width d was varied. Alternatively, also pitch Λ or the height profile could be varied to design a lens.

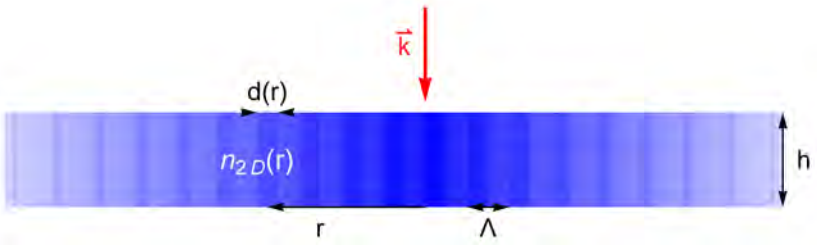

Figure 3.4: Schematics of a flat transmissive lens design based on effective medium theory. The effective refractive index n_{2D} was changed with radius r, by varying the width d of the grating pillars and holes with pitch Λ and height h. The lens was designed for plane wave incidence with a wave vector $\vec{k}$.

Using the basic correspondence between the optical path length and the accumulated phase [12], the difference in effective refractive index Δn was linked to the phase ϕ, that is accumulated when passing through a layer with thickness h

$$\phi(r) = \frac{2\pi}{\lambda}\Delta n(r)h. \tag{3.10}$$

This gives the height h necessary for changing the transmitted phase ϕ over 2π

$$h = \frac{\lambda}{\Delta n_{max}}. \tag{3.11}$$

For the design with silicon pillars and holes etched into silicon, the necessary height of the grating layer was $h = 4.3$ μm. Inserting the effective refractive index $n_{2D}(d)$ from Equation 3.5 and the necessary phase for a lens derived from the Huygens-Fresnel principle $\phi(r)$ from Equation 2.8 into Equation 3.10, gives an implicit relation for $d(r)$

$$n_{2D}(d) = n_{min} + \frac{1}{h}\frac{\lambda}{2\pi}\phi(r). \tag{3.12}$$

The width function $d(r)$ for the design of a lens was obtained from the above equation by numerically solving for the width d for a specific radius r.

3.4 Wave-optics simulation of a lens design based on EMT

A finite element simulation with Comsol Multiphysics was used to do a wave-optics simulation of the transmissive lens design based on effective medium theory described above. For more information on the FEM method for electromagnetics see e.g. Section 4.1.2 and Reference [16].

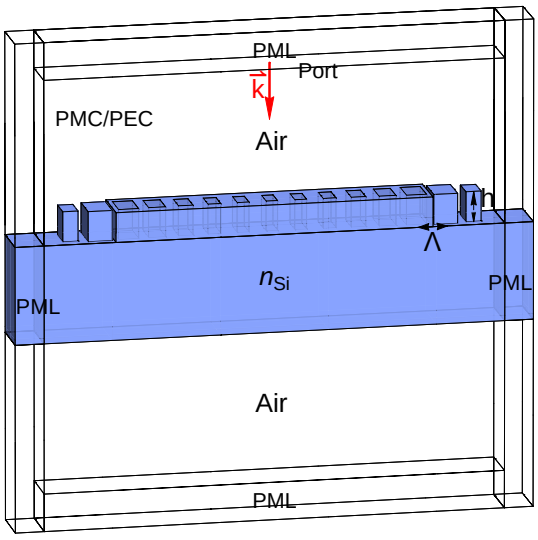

Figure 3.5: Geometry for the wave-optics simulation of a lens design based on effective medium theory. The port was the source of a plane wave with wave vector $\vec{k}$. The transmissive lens consisted of silicon pillars and holes etched into silicon with a pitch Λ, a height h and a width $d(x)$ depending on the distance from the center of the lens x. The transmissive lens was placed on a silicon substrate with thickness t. The simulation region was surrounded by perfectly matched layer (PML) boundary conditions on four sides. On the remaining two sides, perfect electric conductor (PEC) boundary conditions were used.

Figure 3.5 shows the geometry used for the FEM simulation. A so-called *port* was used to launch a plane wave with wave vector $\vec{k}$ into the simulation region. The transmissive lens consisted of silicon pillars and holes with constant pitch Λ and height h. The width $d(x)$ was obtained by numerically solving the implicit Equation 3.12 for d, where x was the distance from the center of the lens. Perfectly matched layers (PML) were placed on four sides of the simulation region as absorbing boundary conditions. On the remaining two sides perfect electric conductor (PEC) conditions were used to periodically extend the simulation region.

By using linear discretization order and further simulating only a slab with thickness $\Lambda/2$, the simulation effort could be reduced significantly. The drawback of the simulation set-up was, that all simulations were for a lens, which focuses on a line. In practice, focusing on a point would be more relevant. Due to the two-dimensional grating it is not possible to do a 2D simulation with rotational symmetry. But for a demonstration of principle and basic investigations, the simulated lens can serve as a close approximation of a cut along the optical axis of a lens focusing on a point.

Figure 3.6 shows the results of a wave-optics simulation with the geometry described above. Equation 2.8 was used to find the phase function for a lens with a substrate thickness of $t = 200$ μm and a focal length of $f = 700$ μm. The color scale in Figure 3.6 shows the normalized magnitude of the Poynting vector, for plane wave incidence with wave vector $\vec{k}$. It was observed, that there is a second focal spot around 400 μm from the lens plane, caused by light being reflected two times at the interfaces of the silicon substrate.

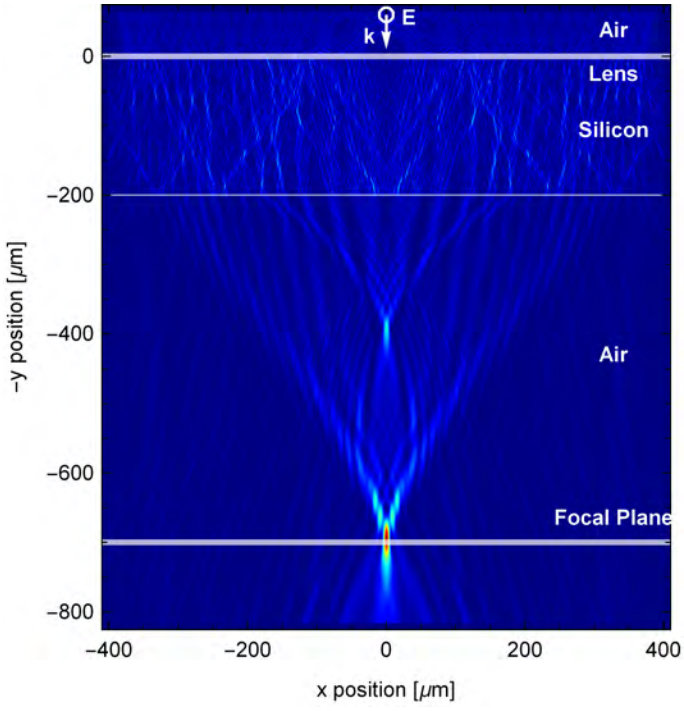

Figure 3.6: Results of the wave-optics simulation of a EMT lens design for a wavelength of $\lambda = 10$ μm. The color scale shows the normalized magnitude of the Poynting vector. A distinct focal spot was observed at a distance of $f = 700$ μm from the lens plane.

Figure 3.7 shows the main focal point at a distance of $f = 700$ μm from the lens plane in more detail. A cut along the optical axis in Figure 3.7a and in the focal plane in Figure 3.7b reveal that the maximum is not exactly at a distance of 700 μm. Also, there are distinct

side-peaks next to the focal spot. The wave-optics simulations show that the devised lens design based on effective medium theory should work in principle, but there are some drawbacks. First, the maximum aspect ratio of the above design is around 1:11. For mass-scale production with standard lithographic processes this is a rather high value [4]. Secondly, by using a large Δn_{max} the transmittance is reduced. Ideally, a material with an effective refractive index between silicon and air and a thickness of $\lambda/4$ would serve as an anti-reflective coating [12]. However, without varying the effective index no lens effect can be achieved.

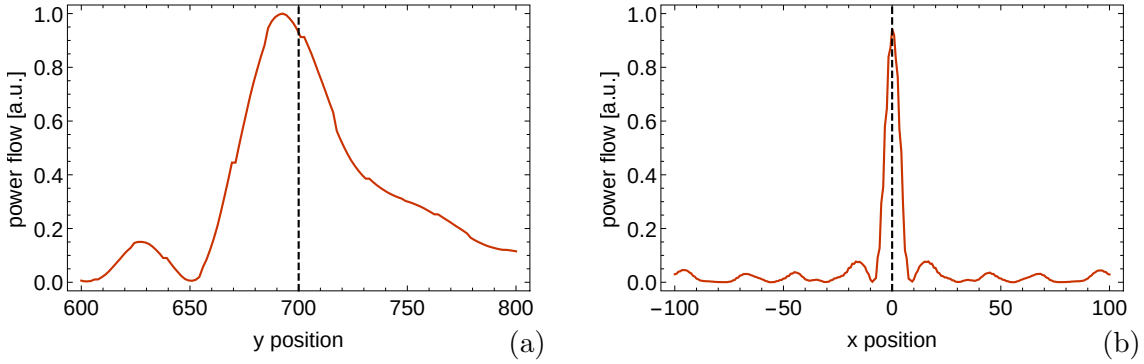

Figure 3.7: Cut along the optical axis (a) and in the focal plane (b), showing the normalized magnitude of the Poynting vector.

To overcome the limitation of a rather large aspect ratio and increase the transmission, sub-wavelength gratings were investigated. These structures have a larger ratio of grating pitch to wavelength $\Lambda/\lambda \sim 1$, for which the effective medium theory is not valid any more.

4 DESIGN OF A SUB-WAVELENGTH GRATING LENS

Sub-wavelength grating structures were designed for wavelengths of 4 μm and 10 μm using finite difference time domain and finite element simulations. To change the transmitted phase in a range from 0 to 2π, the necessary aspect ratio of the devised structures was below 1:5. However, the investigation of the behavior for off-axis incidence of light revealed, that unwanted lateral modes are also supported by the grating structure. Another result of the simulations was, that even for these structures with a ratio of grating pitch Λ to wavelength λ below 1, Fraunhofer far field diffraction theory accurately describes the onset of scattering into higher orders.

4.1 Simulation methodology

Gratings with a large ratio of pitch Λ to wavelength λ are described by Fraunhofer far field diffraction theory [12]. For a small ratio of Λ/λ an effective medium approach can be used [9]. But gratings with $\Lambda \sim \lambda$ are difficult to treat analytically. Neither Fraunhofer diffraction theory nor an effective medium approach can fully describe the observed properties of broadband high reflection or transmission [10]. Due to the importance of the interaction between local geometry and electromagnetic field, it is necessary to solve Maxwell's equations. So with the exception of simple geometries, where an analytical solution is possible [17], this means that one has to utilize the methods of computational electrodynamics to find a numerical solution.

Since methods for computational electrodynamics are of great scientific and commercial interest, a variety of methods and implementations have been developed. For the simulation of the grating structures in this work, the Finite Difference Time Domain method (FDTD) and the Finite Element Method (FEM) were used.

4.1.1 Finite Difference Time Domain (FDTD)

For a finite difference time domain simulation Maxwell's curl equations in an isotropic medium without charge transport

$$\begin{aligned} \frac{\partial \vec{B}}{\partial t} + \nabla \times \vec{E} &= 0, \\ \frac{\partial \vec{D}}{\partial t} - \nabla \times \vec{H} &= 0, \\ \vec{B} &= \mu \vec{H}, \\ \vec{D} &= \epsilon \vec{E} \end{aligned} \tag{4.1}$$

are discretized on a spatial and temporal grid according to a scheme devised by K. Yee in 1966 [18]. In the Yee-algorithm both the spatial and temporal grid for electric and magnetic field are staggered for enhanced accuracy. By default modern FDTD solvers interpolate the data to the origin of the grid point, so there is no issue for the analysis of the results. For a detailed introduction to the FDTD method see e.g. Reference [19].

For the spatial domain discretization the FDTD method uses a rectangular grid. To avoid aliasing effects both the temporal and the spatial grid have to be fine enough to sample the highest occurring frequencies. Because FDTD is a time-domain method, it is especially suited to simulate the behavior for multiple frequencies in a single simulation run. The downside of the method is mainly that in order to obtain an accurate frequency domain field distribution, a rather long simulation time is necessary. Especially when resonance effects occur, this can significantly increase the simulation effort.

4.1.2 Finite Element Method (FEM)

For a frequency domain finite element simulation a time-harmonic ansatz is made for the electric field

$$\vec{E}(\vec{r},t) = \Re\left(\tilde{\vec{E}}(\vec{r})e^{-i\omega t}\right). \tag{4.2}$$

The governing wave equation for the phasor $\tilde{\vec{E}}$ can be written in the form

$$\nabla \times \left(\frac{1}{\mu}\nabla \times \tilde{\vec{E}}\right) - \omega^2 \epsilon \tilde{\vec{E}} = \vec{0}. \tag{4.3}$$

For the FEM simulation the spatial domain of the boundary value problem is discretized using sub-domain elements. The wave equation is applied to each of these finite elements, after it is brought to the *weak* integro-differential form. Interpolation functions are used for the unknown $\tilde{\vec{E}}$ in the element domain, resulting in a set of linear equations. A system matrix is then assembled for the whole spatial domain, which can be solved by direct or iterative numerical methods. For a detailed introduction to the FEM method for electromagnetics see e.g. Reference [16].

The spatial domain discretization, usually referred to as a *mesh*, for the FEM simulation is not limited to rectangular grids. For three-dimensional simulations usually a tetrahedral mesh is used. The minimum element size and the order of the interpolation function have to be chosen appropriately for the frequency ω in order to avoid aliasing effects. To speed up the creation of the mesh it can be advantageous to use a combination of a tetrahedral mesh and more general polyhedral spatial discretization.

A downside of the frequency domain FEM simulation compared to FDTD is that a solution is obtained for the phasor $\tilde{\vec{E}}(\vec{r})$ rather than the electric Field $\vec{E}(\vec{r},t)$. But when the time-harmonic ansatz in Equation 4.2 is valid, FEM is an accurate and time-efficient simulation method to obtain frequency domain field profiles.

4.1.3 Perfectly Matched Layer (PML) and Bloch boundary condition

Both FDTD and FEM programs offer the use of Perfectly Matched Layers (PML) to simulate open boundaries conditions [20]. The PML is an artificial layer, which attenuates the fields by reformulation of the respective field equations. The main advantage of a PML compared to other absorbing boundary conditions is that the reflection of the outgoing waves is prevented over a range of incidence angles.

Bloch boundary conditions have to be used in FDTD and FEM simulations when simulating a periodic structure with periodic electromagnetic fields, but a phase shift between the periods. This is for example the case for plane wave incidence at an angle or for the simulation of different diffraction orders [21].

4.2 Geometry and set-up of the simulation

Having programs for FDTD (Lumerical FDTD Solutions) and FEM (Comsol Multiphysics) allowed for the comparison of the results and the use of the computationally most efficient method for a particular simulation task. The geometry shown in Figure 4.1 was used for the design of the sub-wavelength grating lens in both programs. The structure consisted of cylindrical pillars with height h and diameter d, made of a dielectric material with a refractive index n_1. The pillars were placed on a substrate material with refractive index n_2. Perfectly matched layers were placed on top and bottom of the simulation region. On the remaining four faces Bloch boundary conditions were used, which are called Floquet

boundary conditions in Comsol Multiphysics, to simulate a periodic structure with grating pitch Λ.

For the incident wave with wave vector $\vec{k}$, a plane wave source was used in FDTD Solutions. Comsol Multiphysics uses so called *ports* to simulate an incident wave, which also allow the monitoring of transmitted and reflected radiation. Ports were placed between the perfectly matched layers and the other simulation region above and below the grating structure. In FDTD Solutions, frequency domain monitors were used to monitor the transmitted and reflected radiation.

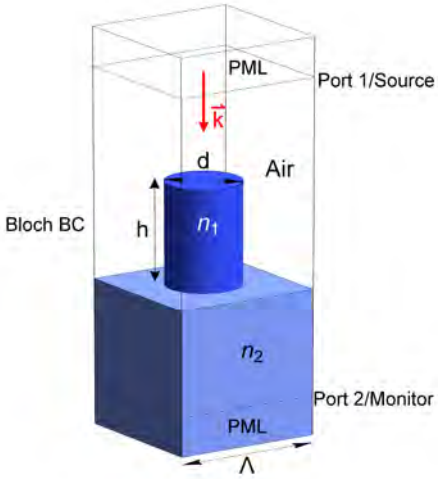

Figure 4.1: Geometry for the simulation of the sub-wavelength grating. The structure consisted of cylindrical silicon pillars with height h and diameter d placed on a substrate material. A plane wave with wave vector $\vec{k}$ was incident from the top and transmitted and reflected radiation were monitored. On the top and the bottom of the simulation region Perfectly Matched Layers (PML) were placed to attenuate the fields. Bloch boundary conditions were introduced on the remaining four sides effecting periodicity with pitch Λ.

In Comsol Multiphysics the transmitted power was calculated from the S_{21} parameter, which is obtained according to

$$S_{21} = \frac{\int_{\Omega_2} \vec{E}_c \cdot \vec{E}_2^* \, \mathrm{d}A_2}{\int_{\Omega_2} \vec{E}_2 \cdot \vec{E}_2^* \, \mathrm{d}A_2}, \tag{4.4}$$

when two ports are placed in the electromagnetic simulation. In this formulation $\vec{E}_2$ is the electric field of the eigenmode in port 2, this was assumed to be a plane wave. $\vec{E}_c$ is the calculated field in port 2. The transmitted power T was then calculated according to

$$T = |S_{21}|^2. \tag{4.5}$$

The transmitted phase ϕ was calculated as the angle of the complex S_{21} parameter

$$\phi = \tan^{-1} \frac{\Im(S_{21})}{\Re(S_{21})}. \tag{4.6}$$

FDTD Solutions uses sources and frequency domain monitors instead of ports. The transmitted and reflected power were directly extracted from monitors placed between the PMLs and the rest of the simulation region. For the transmitted phase separate point

monitors placed in the center of the 2D monitors were used. This method also assumes that the exiting wave is a plane wave, calculating the S_{21} parameter from

$$S_{21} = \frac{E_t}{E_i}, \tag{4.7}$$

where E_t is the transmitted and E_i is the incident electric field component at the point monitors. The transmitted phase ϕ was calculated from Equation 4.6.

4.3 Lens design for a wavelength of 4 μm

The first lens based on the sub-wavelength grating principle was designed to work in the MIR window around a design wavelength of $\lambda = 4$ μm. The structure consisted of a square array of cylindrical silicon pillars placed on a sapphire substrate with a unit cell according to the geometry in Figure 4.1. The choice of materials takes advantage of the difference in refractive index of silicon $n_{Si} = 3.4294$ and sapphire $n_{Al_2O_3} = 1.674$, as well as the high transmission of sapphire at the design wavelength [15]. Equation 2.1, which was derived from the Huygens-Fresnel principle, was used to find the phase ϕ at radius r to build a lens with focal length f. The results of FDTD simulations shown below were used to link the geometric parameters of the grating to the transmitted phase.

4.3.1 Finding values for the grating parameters

In order to find suitable values for the height h, pitch Λ and diameter d of the silicon pillars, several parameter sweeps and optimization runs were done with the set-up of the FDTD simulation described above. For the lens design, the pitch was held constant while the fill factor, which is the ratio diameter/pitch, was varied to change the transmitted phase. The goal of the sweeps and optimization runs was to find a region in the phase space, where the transmitted phase could be changed over 2π while the transmitted power remained as high as possible. As an additional condition the maximum aspect ratio of the grating features had to be kept as small as possible. Results shown in Figure 4.2-4.4 suggested to use a pillar height of $h = 2.6$ μm, a pitch of $\Lambda = 1.8$ μm and a fill factor varying between 30% and 70% for the lens design. A sub-wavelength grating lens designed with these parameter values has a maximum aspect ratio smaller than 1:5.

Figure 4.2 shows the power transmitted into the zeroth diffraction order and the respective transmitted phase for two cuts in the phase space of the grating parameters. The values chosen for the lens design are marked by a box. It can be seen that for both a constant height in (a) and a constant pitch in (b), regions of high and low transmitted power exist in close proximity. This has implications for the sensitivity of a lens built according to this design. It is desirable that small deviations of the grating geometry caused by inaccuracy in production do not change the lens performance significantly, i.e. the sensitivity of the lens performance with respect to the values of the grating parameters is low. To ensure that this additional constraint is met, the values for the grating parameters were chosen so they would lie in the center of regions of high transmitted power.

There also is a drop in the transmitted power for a grating pitch lager than 2.5 μm in Figure 4.2a, which is caused by scattering into higher diffraction orders. The transmitted phase in Figure 4.2c-d appears to be a smooth function of the fill factor for the chosen values of height and pitch. However, discontinuities are observed along directions that correspond to rapid changes of the transmitted power in Figure 4.2a-b.

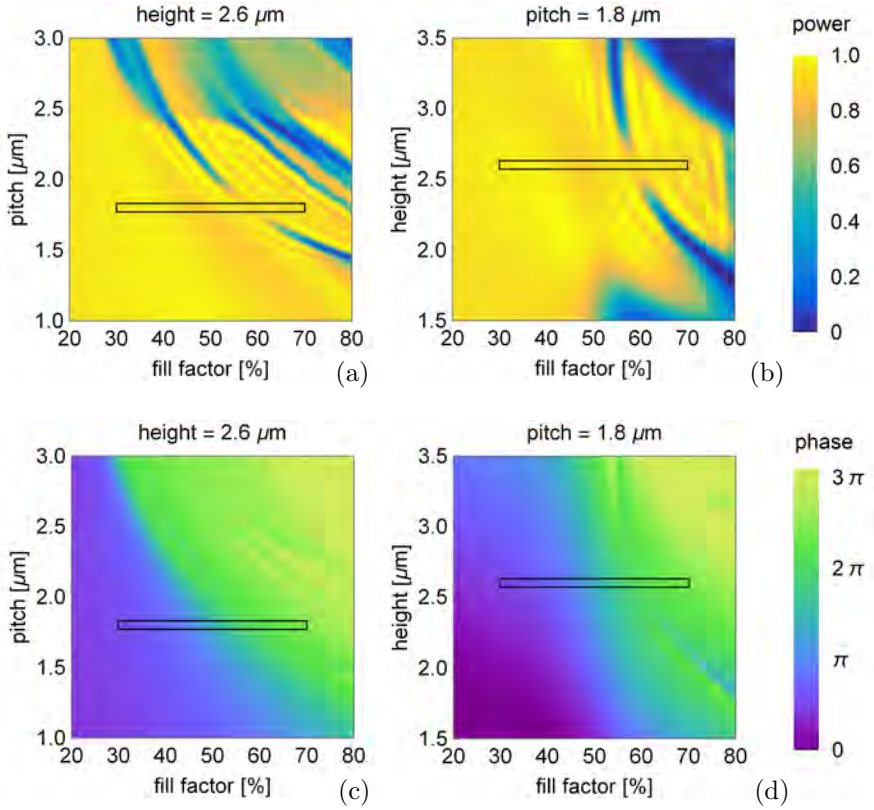

Figure 4.2: Cut planes in phase space with a box marking the chosen values for grating parameters showing transmitted power (a,b) and phase (c,d). Fixed height of 2.6 μm with varying pitch and fill factor in (a) and (c). Fixed pitch of 1.8 μm with varying height and fill factor in (b) and (d).

Figure 4.3a gives evidence of broadband high transmission around the design wavelength. It is observed that there is a drop in the transmitted power for shorter wavelengths and larger fill factor, which has to be taken into account when designing a lens for a certain wavelength band. Also the transmitted phase in Figure 4.3b changes with the wavelength. This further restricts the width of the wavelength band for which a sub-wavelength grating lens can show good performance.

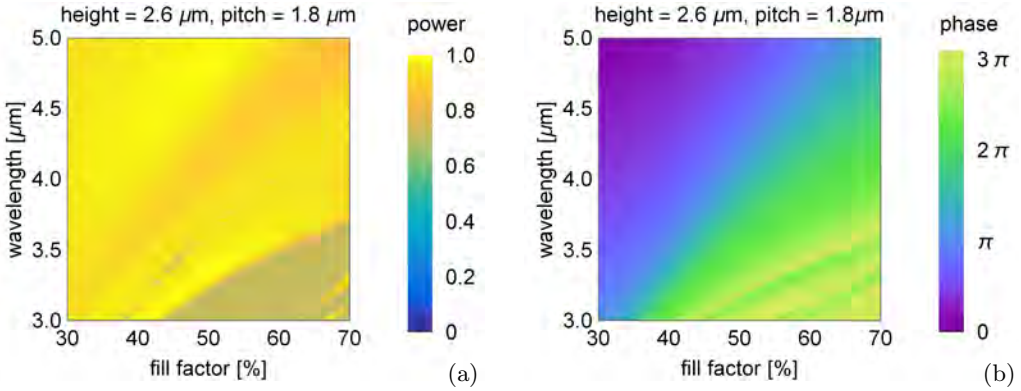

Figure 4.3: Wavelength dependence of the transmitted power (a) and phase (b) for fixed height of 2.6 μm and pitch of 1.8 μm indicates broadband transmission around the design wavelength of $\lambda = 4$ μm.

The plots in Figure 4.4a show $> 90\%$ transmitted power for several wavelengths and Figure 4.4b illustrates the change of the transmitted phase with the incident wavelength. The

phase function for the design wavelength of $\lambda = 4$ μm was fitted with a 8^{th} order polynomial, giving a usable correspondence between fill factor and the phase ϕ. By inserting $\phi(d/\Lambda)$ into Equation 2.1 a design criterion for a sub-wavelength lens was obtained.

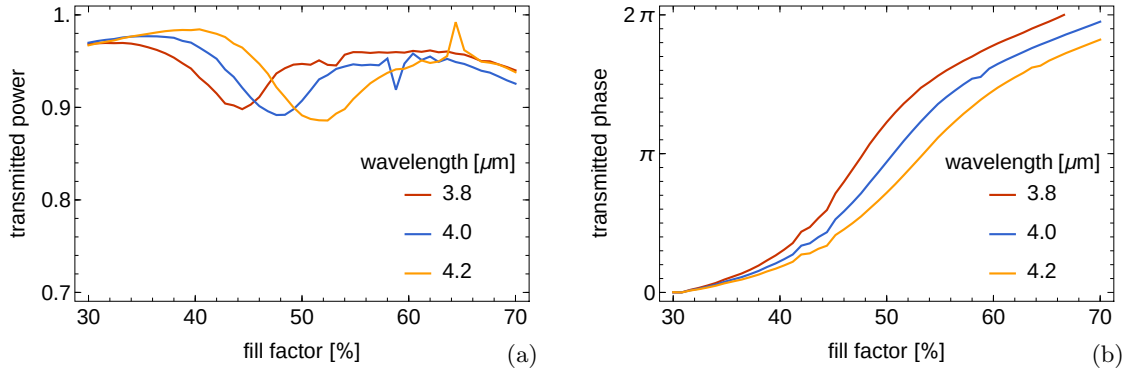

Figure 4.4: Transmitted power (a) and phase (b) for and several wavelengths in dependence of the fill factor. The transmitted phase for the design wavelength of $\lambda = 4$ μm was fitted with a 8^{th} order polynomial to give a usable correspondence between fill factor and phase ϕ.

4.3.2 Multi-mode propagation in the grating

The extraordinary properties of sub-wavelength high contrast gratings such as broadband high reflection have been described by multi-mode propagation inside the grating [17]. The basic idea is, that while only the zeroth order is able to propagate outside the grating, several modes can be excited inside the grating. These modes couple at the interfaces between the grating and the surrounding material with strong dependence on geometry and refractive index, explaining the extraordinary transmission properties. The electric field and the power transport inside the cylindrical grating pillars in Figure 4.5 can also be interpreted by using this concept.

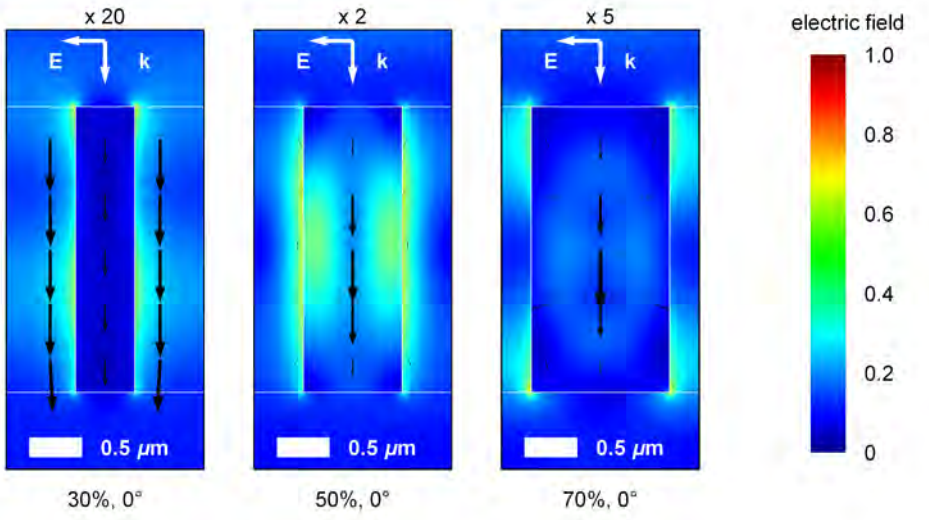

Figure 4.5: Electric field (color scale) and power transport (arrows) inside the grating for normal incidence. Note that the arrows displaying the direction and magnitude of the Pointing vector have different scale, which is specified by the values above.

The plots in Figure 4.5 are the result of a frequency domain FEM simulation in Comsol Multiphysics with quadratic discretization order. Plots from frequency domain monitors

in FDTD Solutions qualitatively showed the same results. For a fill factor of 30% and normal incidence, the electric field (color scale) inside the silicon pillars is low and the energy transport indicated by the Poynting vector (arrows) occurs mainly in air. For a fill factor of 50% there is an increased electric field inside the silicon pillars and also the energy transport is mainly in the silicon. For a fill factor of 70%, the energy transport almost exclusively occurs inside the silicon pillars.

One interpretation of this observation is that there is a transition of the multi-mode propagation inside the grating [4]. Different modes contribute to the propagation depending on the fill factor of the grating. This transition in the multi-mode propagation is accompanied by a phase change over 2π observed in Figure 4.4b. Note that for better visibility the lengths of the arrows indicating the magnitude of the Poynting vector are scaled for the different fill factors. The normalization of the electric field and magnitude of the Poynting vector in Figure 4.5 is the same as in Figure 4.8 and Figure 4.9 for comparability.

4.3.3 Changing the incidence angle

The simulations above were all done for normal incidence. For imaging purposes it is indispensable to also investigate the transmission for larger incidence angles. Results showing the total transmitted power and the transmitted power into zeroth diffraction order for different incidence angles and different polarization can be found in Figure 4.6. It is clearly seen that for TE polarized light in Figure 4.6a, transmission into higher diffraction orders occurs for incidence angles exceeding a certain value for a fill factor of 50%, but is barely visible for 30%. For TM polarized light in Figure 4.6b transmission into higher diffraction orders also occurs for a fill factor of 30%. But an even more prominent feature in the plot for TM polarized light is the drop to zero transmitted power for a fill factor of 50% and an incidence angle of approximately 30 degrees. For larger incidence angles the total transmitted power goes up again, but the transmission into the zeroth order stays below 20%. To get a better understanding of the origin of the observed transmission behavior a more detailed investigation was done.

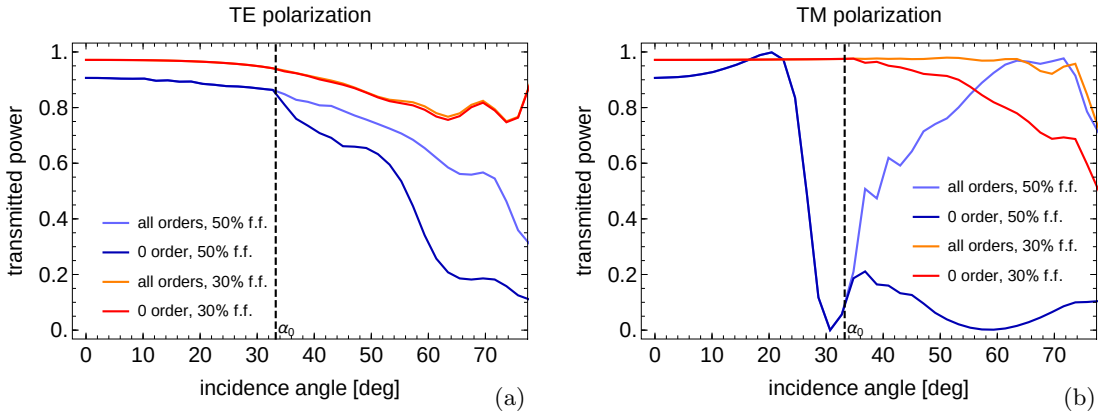

Figure 4.6: Transmitted power for different incident angles. Scattering into higher diffraction orders for incidence angles larger than α_0 for the TE polarization and a fill factor of 50% (a), scattering into higher orders as well a drop to zero transmission for the TM polarization and a fill factor of 50% at an incidence angle of 30°(b).

4.3.4 Scattering into higher diffraction orders

The transmission behavior in Figure 4.6 shows that the maximum incidence angle of a sub-wavelength grating lens with the design devised above is limited by transmission into higher diffraction orders. This basic limitation can be explained by Fraunhofer diffraction theory [12].

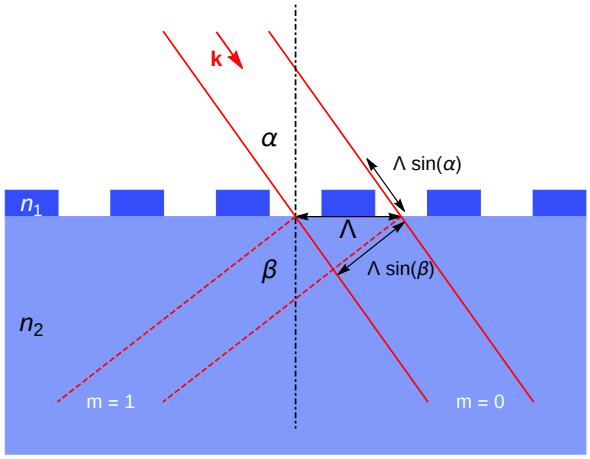

Figure 4.7: Illustration of scattering into higher diffraction orders as predicted by Fraunhofer diffraction theory. A plane wave with wave vector $\vec{k}$ has an incidence angle α and a diffraction maximum of order $m = 1$ is observed at an angle β.

Considering a plane wave with wave vector $\vec{k}$ incident on a grating with pitch Λ, as it is sketched in Figure 4.7, one can derive the incidence angle α for transmission into higher orders. For a diffraction maximum to occur at an angle β, the difference in optical path lengths of two rays with separation Λ in the grating plane, has to be a multiple of λ

$$\Lambda \left(\sin(\alpha) + n_2 \sin(\beta)\right) = m\lambda, \qquad m \in \mathbb{Z}. \tag{4.8}$$

For $\beta = \frac{\pi}{2}$, $n_2 = n_{Al_2O_3}$ and $m = 1$ this turns into the expression for the angle α_0 shown as a dashed line in Figure 4.6

$$\alpha_0 = \sin^{-1}\left(\frac{\lambda}{\Lambda} - n_{Al_2O_3}\right), \tag{4.9}$$

which is the minimum angle for transmission into higher diffraction orders according to Fraunhofer far field diffraction theory. The angle calculated with Equation 4.9 matches the angle, where a difference in the behavior of total transmission and transmission into zeroth order starts to appear in Figure 4.6. The results from simulations for substrates with different refractive index also matches the respective theoretical value. So to increase transmission one could therefore change the substrate material. A more practicable approach would be to find a grating structure with reduced pitch. Unfortunately this would in turn increase the necessary aspect ratio.

Electric field and energy transport inside the grating were investigated, to get a better understanding of why the transmission behavior differs for the TE and the TM polarization. Transmission into higher orders in Figure 4.6 is low for a fill factor of 30% and the TE polarization, but larger for the TM polarization. The respective plots obtained by FEM simulation in Figure 4.8 for an incidence angle of 50° show a different direction of the energy transport inside the silicon pillar and in air. For the TE polarization the electric field is low. In the plane where the transmitted wave exits the grating, the direction and

magnitude of the Poynting vector is similar in- and outside the silicon pillars. For the TM polarization, there is a large field at some parts of the cylinder edges. In the exit plane the Poynting vector has different magnitude and direction in- and outside the grating pillars. Considering the basic requirement of either periodic phase or amplitude modulation for a diffraction grating [12], this observation was linked to the transmission behavior.

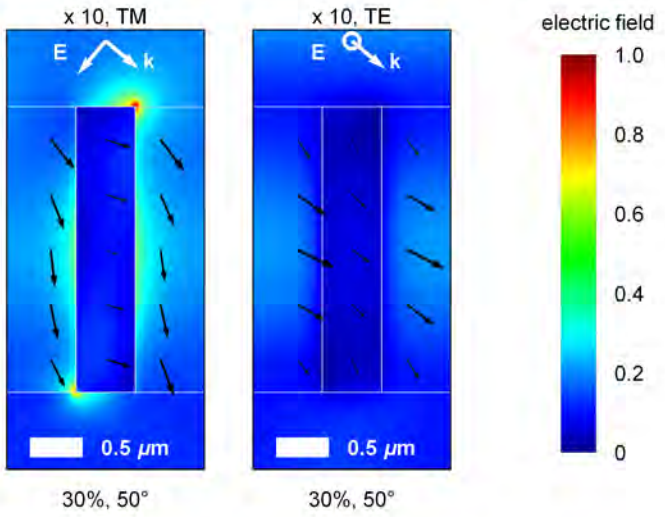

Figure 4.8: Electric field (color scale) and power transport (arrows) inside the grating for TM and TE polarized incidence at an angle of 50°. Note that the arrows displaying the direction and magnitude of the Pointing vector have different scale, which is specified by the values above.

For the TE polarization there is only minor modulation of amplitude in the exit plane indicated by a similar Poynting vector. Qualitatively this is in agreement with the observation of low transmitted power into higher diffraction orders for the TE polarization in Figure 4.6. For the TM polarization the modulation in the exit plane is more pronounced, causing increased scattering into higher diffraction orders.

4.3.5 Excitation of Lateral modes

For a fill factor of 50% and TM polarized incidence, a drop to zero for transmitted power is shown in Figure 4.6b. The plot of electric field and power transport in Figure 4.9 shows that this effect is accompanied by a large electric field, indicating a resonance effect. In addition the Pointing vector is, contrary to the other cases, pointing in lateral direction, suggesting that a lateral mode is excited inside the grating.

The plot of the normalized transmitted power and phase depending on the fill factor for an incidence angle of 30° in Figure 4.10 further supports the assumption that a resonant mode is excited for a fill factor of 50%. Typically for a resonance effect, the drop to zero transmission is accompanied by a discontinuity of the transmitted phase. While the loss of transmission is undesirable for focusing purposes, the excitation of a lateral mode could be utilized to build a grating coupler for integrated photonic circuits [3].

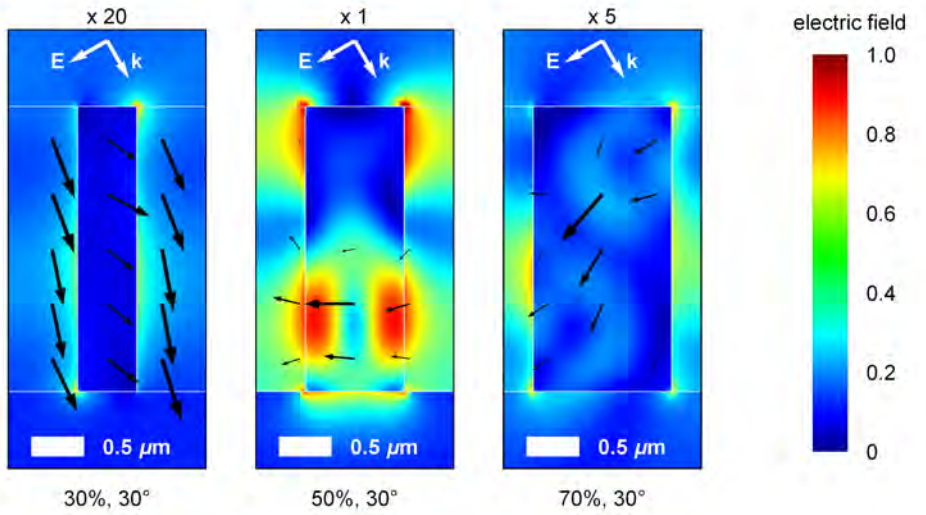

Figure 4.9: Electric field (color scale) and power transport (arrows) inside the grating for TM polarized incidence at an angle of 30°. Note that the arrows displaying the direction and magnitude of the Pointing vector have different scale, which is specified by the values above.

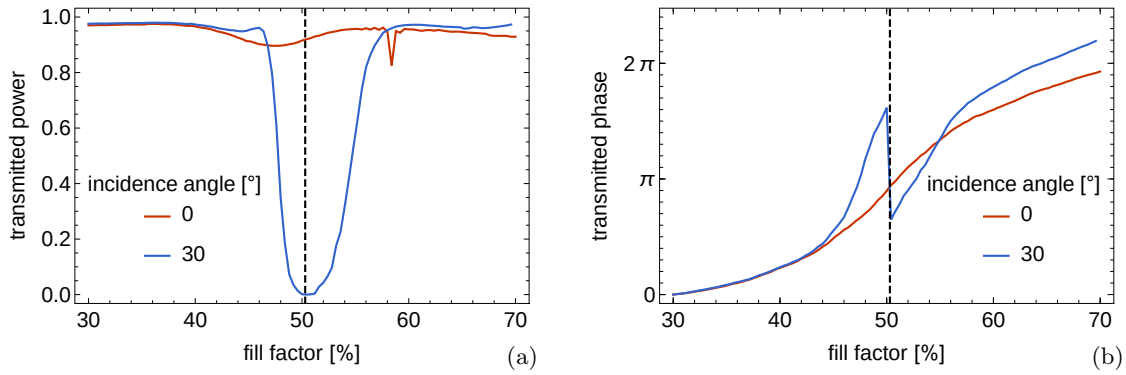

Figure 4.10: Total transmitted power (a) and phase (b) for several incidence angles and the TM polarization in dependence of the fill factor for the design wavelength of $\lambda = 4$ μm.

4.3.6 Resonance effects for TE polarized incidence

The results in Figure 4.6 and Figure 4.10 suggest, that better lens performance for incidence angles $> 30°$ could be achieved by using only TE polarized light. Unfortunately, resonance effects also occur for TE polarized incidence, as it can be seen in Figure 4.11. There are drops in the total transmitted power for fill factors of around 54%, 58% and 62% for an incidence angle of 30° in Figure 4.11a. The drops in the transmitted power are accompanied by discontinuities in the transmitted phase seen in Figure 4.11b. However, compared to the resonance effect for the TM polarization in Figure 4.10a, the resonance effects for the TE polarization in Figure 4.11a are narrower, meaning that low transmission only occurs for a specific fill factor.

It is also observed from Figure 4.11b, that in addition to jumps in the transmitted phase, also the general shape of the transmitted phase $\phi(d/\Lambda)$ is slightly changed. This should be taken into account when designing a lens for off-axis incidence according to Equation 2.1.

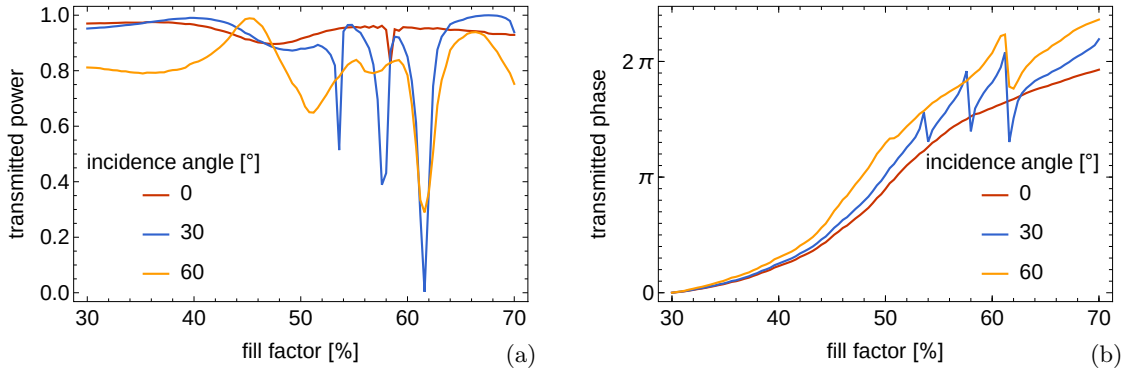

Figure 4.11: Total transmitted power (a) and phase (b) for several incidence angles and the TE polarization in dependence of the fill factor for the design wavelength of $\lambda = 4$ μm.

The implications of the resonance effects, observed in the simulations presented above, are not completely clear. For the design of the sub-wavelength grating lens, all the pillars of the simulated structure had exactly the same diameter. But in order to build an actual lens, the diameter of the pillars had to be varied. This was expected to hinder the excitation of lateral modes, because of the disturbed periodic structure.

Simulations of the full lens design in Chapter 5 show, that imaging at large incidence angles is possible for the TE and the TM polarization, despite the resonance effects observed, when designing the grating structure.

4.4 Lens designs for a wavelength of 10 μm

Designing a sub-wavelength grating lens for a wavelength of $\lambda = 10$ μm requires the use of a different substrate material, because sapphire does not provide suitable transparency [15]. Alternative materials would be ZnSe or chalcogenide glasses. However, the simplest and cheapest alternative is to use silicon as a substrate material as well.

4.4.1 Silicon pillars on a silicon substrate

A large contrast in refractive index is required between substrate material and the grating itself, to observe effects of broadband high reflection or transmission for high-contrast dielectric gratings [10]. Using silicon as substrate material and for the grating pillars was therefore expected to reduce the transmitted power. Two designs with different pitch Λ and range of the fill factor were simulated. In the first design A, the pillars had a pitch of $\Lambda = 4.5$ μm, a height of $h = 6.25$ μm and the fill factor was varied between 20% and 70% for a 2π change in the transmitted phase. The maximum aspect ratio of this design was below 1:7. The results of FEM simulations for several wavelengths are shown in Figure 4.12. There is a reduction of the transmitted power to an average of 69% for the design wavelength, compared to a value of 94% for a sapphire substrate and a design wavelength of $\lambda = 4$ μm in Figure 4.4.

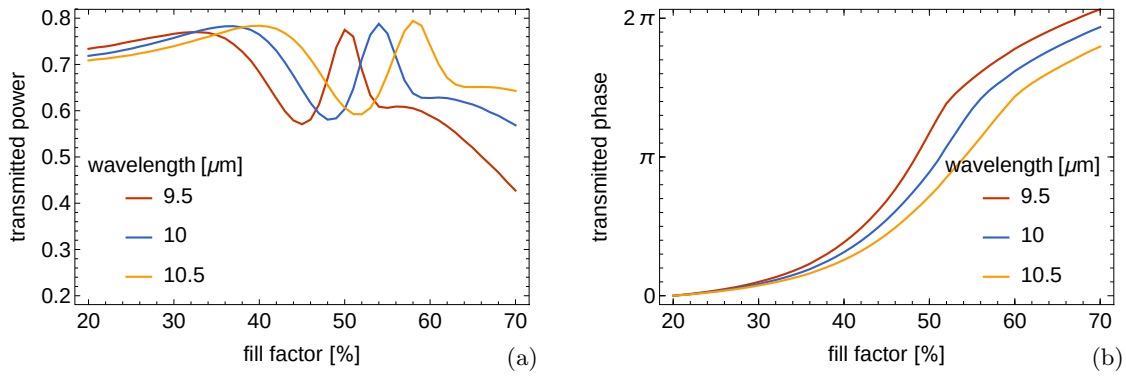

Figure 4.12: Transmitted power (a) and phase (b) for several wavelengths in dependence of the fill factor for design A. The pitch of the silicon pillars was 4.5 μm, the height 6.25 μm. The transmitted phase for the design wavelength of $\lambda = 10$ μm was fitted with a 8^{th} order polynomial to give a usable correspondence between fill factor and phase ϕ.

For the second design B, a pitch of $\Lambda = 5$ μm and a height of h = 6.25 μm were used, while the fill factor was varied between 30% and 70%. The maximum aspect ratio of this design was approximately 1:4 and the average transmitted power for the design wavelength was reduced to 63%. Results of FEM simulations for different wavelengths are shown in Figure 4.13. The advantage of a reduced aspect ratio compared to the first design A comes at the cost of a reduced average transmitted power.

To evaluate the feasibility of a sub-wavelength grating lens, samples with different focal length were built using the grating dimensions and the $\phi(d/\Lambda)$ relation from design A and B. Detailed simulations of the expected lens behavior can be found in Section 5.4. Different lens designs were placed on a test-chip and evaluated with a dedicated measurement set-up. For more information on the production of sub-wavelength grating lenses and the measurement set-up see Chapter 6.

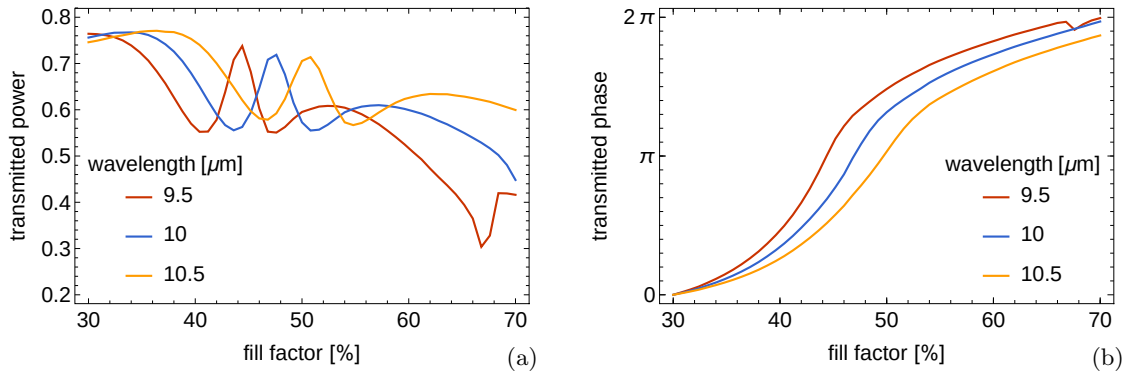

Figure 4.13: Transmitted power (a) and phase (b) for several wavelengths in dependence of the fill factor for design B. The pitch of the silicon pillars was 5 μm, the height 6.25 μm. The transmitted phase for the design wavelength of $\lambda = 10$ μm was fitted with a 8^{th} order polynomial to give a usable correspondence between fill factor and phase ϕ.

4.4.2 Flipped design with silicon pillars on a silicon substrate

For the integration of a lens on wafer level, it can be useful to have a flipped design, meaning that the sub-wavelength grating lens is on the bottom of the substrate. Therefore FEM simulations for the above design A with a pitch of $\Lambda = 4.5$ μm and a pillar height of $h = 6.25$ μm were rerun with an inverted optical path. To do so, the geometry in Figure 4.1 was used and the function of the used ports was simply interchanged. Results shown in Figure 4.14 indicate, that flipping the direction of light propagation does not change the transmission behavior significantly for normal incidence.

When increasing the incidence angle, it was found for the design wavelength of $\lambda = 4$ μm in Section 4.3.4, that even for a grating pitch $\Lambda \sim \lambda$, transmission into higher diffraction orders can be described by Fraunhofer far field diffraction theory. The minimum incidence angle, for which transmission into higher diffraction orders occurs, was calculated according to Equation 4.9. So higher order diffraction is not only dependent on the ratio of grating pitch to wavelength, but also the refractive index of the materials above and below the grating. This means, while the transmission behavior of a flipped design is unchanged for normal incidence, the off-axis transmission is expected to be modified.

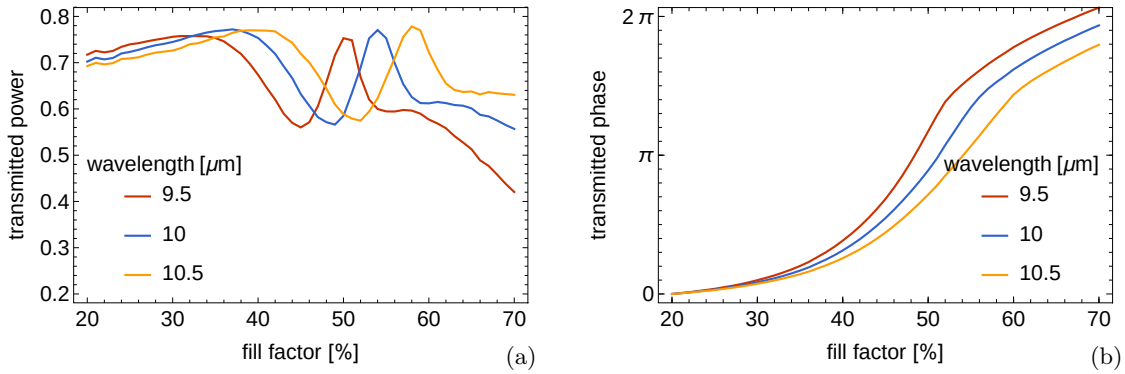

Figure 4.14: Transmitted power (a) and phase (b) for several wavelengths in dependence of the fill factor for design A with inverted optical path. The pitch of the silicon pillars was 4.5 μm, the height 6.25 μm. The transmitted phase for the design wavelength of $\lambda = 10$ μm was fitted with a 8^{th} order polynomial to give a usable correspondence between fill factor and phase ϕ.

4.4.3 Polyethylene on top of silicon pillars on a silicon substrate

Polyethylene provides reasonable transmission around a wavelength of $\lambda = 10$ μm [15] and can therefore be used as a transparent layer or lens material in IR lens design. In one possible implementation, a layer of polyethylene is molded on top of the sub-wavelength grating lens. Simulations with a geometry and set-up according to Figure 4.1, but polyethylene instead of air, showed that the transmission behavior is changed significantly. For the simulation the refractive index $n_{PE} = 1.4$ of commercially available polyethylene [22] was used. In order to change the transmitted phase over 2π, a grating pitch of $\Lambda = 5.2$ μm, a pillar height of $h = 6.3$ μm and a fill factor varied between 25% and 75% were used. Figure 4.15 shows the transmitted power and phase for several wavelengths in dependence of the fill factor. For this design, the maximum aspect ratio was below 1:5 and the average transmitted power was 70%.

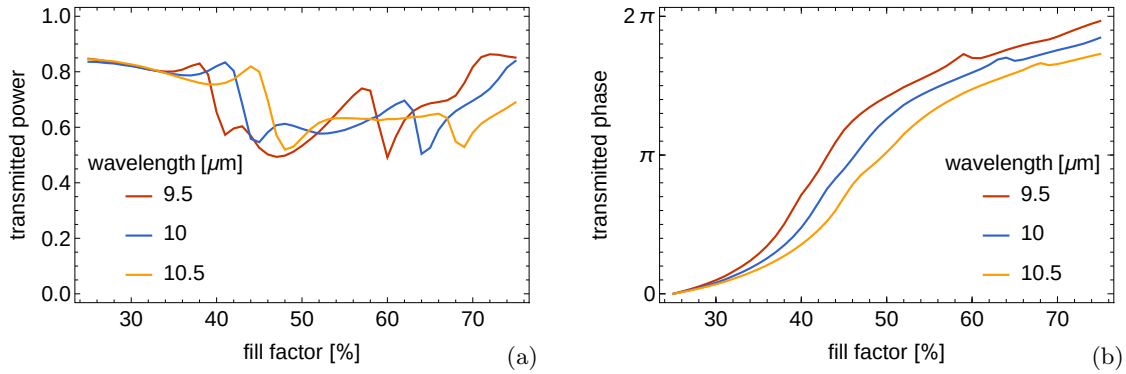

Figure 4.15: Transmitted power (a) and phase (b) for several wavelengths in dependence of the fill factor for a design with polyethylene covering on the silicon pillars. The pitch of the silicon pillars was 5.2 μm, the heights 6.3 μm. The transmitted phase for the design wavelength of $\lambda = 10$ μm was fitted with a 8^{th} order polynomial to give a usable correspondence between fill factor and phase ϕ.

4.4.4 Chalcogenide glass layer between silicon substrate and pillars

In another possible embodiment of a sub-wavelength grating lens for a design wavelength of 10 μm, a layer of material with a lower refractive index was placed between the silicon pillars and the substrate. Figure 4.16 illustrates the modified geometry, with an additional glass layer of thickness t between pillars and substrate.

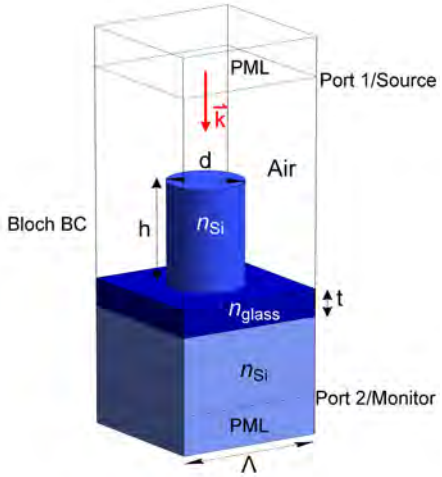

Figure 4.16: Modified geometry for the simulation of the sub-wavelength grating. The structure consisted of cylindrical silicon pillars with height h and diameter d. Between the pillars and the substrate was a glass layer with thickness t. A plane wave with wave vector $\vec{k}$ was incident from the top and transmitted and reflected radiation were monitored. On the top and the bottom of the simulation region Perfectly Matched Layers (PML) were placed, Bloch boundaries on the sides introduced a periodicity Λ.

FEM simulation results for a design with a pitch of $\Lambda = 5$ μm, a pillar height of $h = 6.3$ μm, thickness of the glass layer $t = 1$ μm and the fill factor varying between 30% and 70% are shown in Figure 4.17. The refractive index $n_{glass} = 2.4$ of a commercially available chalcogenide IR glass [15] was used for the glass layer. The thickness t of the glass layer was chosen to be $\lambda_{glass}/4$, the same as for a conventional anti-reflective coating [12], in order to further increase the transmission. With this design, the average transmitted power was 87% and the maximum aspect ratio was around 1:4.

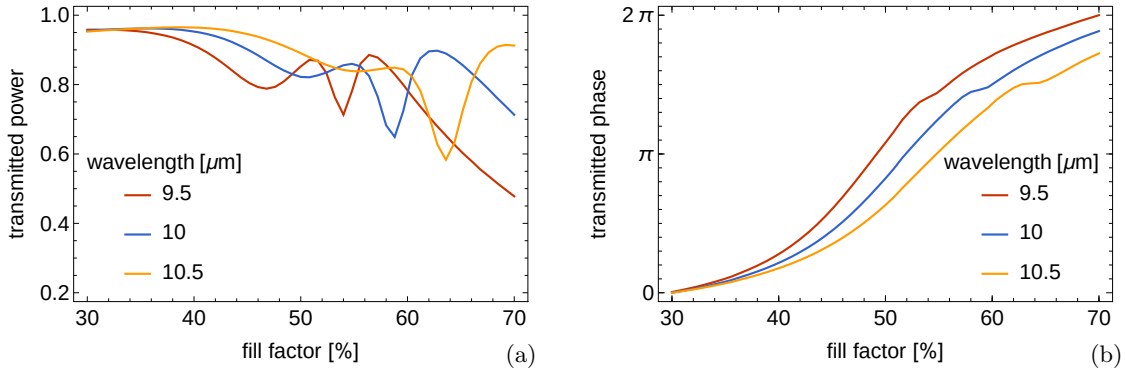

Figure 4.17: Transmitted power (a) and phase (b) for several wavelengths in dependence of the fill factor. The transmitted phase for the design wavelength of $\lambda = 10$ μm was fitted with a 8^{th} order polynomial to give a usable correspondence between fill factor and phase ϕ.

4.4.5 Comparison of the different lens designs

Having a constant high transmission for all fill factors would be ideal for building a lens. The design with silicon pillars on a sapphire substrate for a wavelength of $\lambda = 4$ μm showed an average transmission T of 94% and a standard deviation of 2%. The respective values for different sub-wavelength grating designs and a wavelength of $\lambda = 10$ μm are found in Table 4.1. Because a large contrast in refractive index is required between substrate material and the grating itself, to observe effects of broadband high reflection or transmission [10], it was expected that designs using silicon as substrate show significantly reduced transmitted power. Also, the standard deviation of the transmitted power was increased in comparison to the design for a wavelength of 4 μm. Placing a $\lambda/4$ layer of a chalcogenide IR glass between the silicon pillars and the substrate can improve the transmission significantly, providing a viable option for an improved lens design.

Table 4.1: Comparison of the sub-wavelength lens designs for a wavelength of $\lambda = 10$ μm listing the pitch Λ, pillar height h, average and the standard deviation of the transmitted power T as well as the maximum aspect ratio (AR) for each design.

	Si design A	Si design B	Si design A flip	Si + PE top	Glass layer
Λ [μm]	4.5	5	4.5	5.2	5
h [μm]	6.25	6.25	6.25	6.3	6.3
avg(T) [%]	69	63	68	70	87
std(T) [%]	7	9	7	10	8
max(AR)	1:7	1:4	1:7	1:5	1:4

5 IMAGING DEVICE WAVE-OPTICS SIMULATION

Simple imaging devices using sub-wavelength grating lenses for wavelengths of 4 μm and 10 μm were analyzed by wave-optics simulations. As a main result of this work, it was found that imaging with a field of view greater than 120° should be possible with sub-wavelength grating lenses. Besides chromatic aberrations and behavior for off-axis incidence, the sensitivity of the focusing performance, depending on the fabrication accuracy of the structures was investigated.

5.1 Geometry and set-up of the simulation

A finite element simulation with Comsol Multiphysics was used to do a wave-optics simulation of the sub-wavelength grating lenses designed according to the criteria derived in Chapter 4. Basic guidelines for the construction of an imaging device with a diffractive lens [7] were used to build the geometry for the simulation illustrated in Figure 5.1. The imaging device consisted of an aperture of width a, which was implemented as a smoothed step function in the port condition, and the sub-wavelength grating lens. The port also acted as the source of a plane wave with wave vector $\vec{k}$. The cylindrical grating pillars with pitch Λ and height h had a varying diameter $d(x)$ for a particular lens design, with x being the distance from the center of the lens in x direction. A material with refractive index n_1 was chosen for the pillars placed on top of a substrate with refractive index n_2. Perfectly matched layers (PML) were placed on four sides of sides of the simulation region as absorbing boundary conditions. On the remaining two sides either perfect electric conductor (PEC) or perfect magnetic conductor (PMC) conditions were used, depending on the polarization of the incident plane wave.

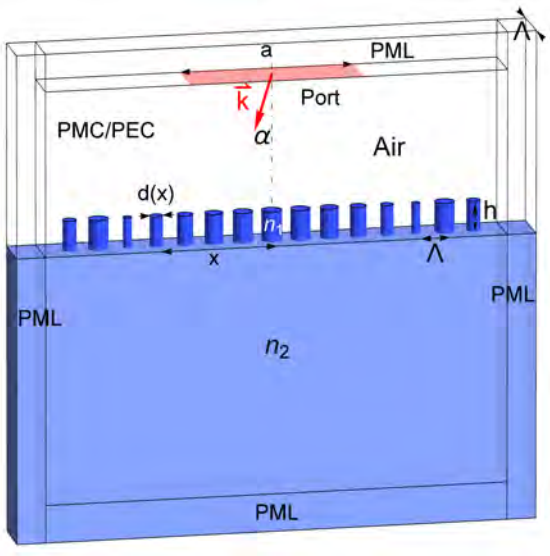

Figure 5.1: Geometry for the simulation of an imaging device. The port is the source of a plane wave with wave vector $\vec{k}$ and incidence angle α. In addition, the port also acts as aperture with width a. The sub-wavelength grating lens consists of cylindrical pillars with pitch Λ, height h and diameter $d(x)$, depending on the distance from the center of the lens x. The pillars of a material with refractive index n_1 are on top of a substrate with refractive index n_2. The simulation region is surrounded by perfectly matched layer (PML) boundary conditions on four sides. On the other two sides, either perfect electric conductor (PEC) or perfect magnetic conductor (PMC) boundary conditions are used, depending on the polarization of the incident plane wave.

By using those boundary conditions, linear discretization order and further simulating only a slab with thickness $\Lambda/2$, the simulation effort could be significantly reduced. The drawback of the simulation set-up was, that all the simulations were for a lens, which focuses on a line. In practice, a lens for an imaging device should rather focus on a point. However, for a demonstration of principle and basic investigations, the simulated lens can serve as a close approximation of a cut along the optical axis of a lens focusing on a point. Naturally, for the optimization of an optical system including astigmatism, one would have to turn to a full simulation of the actual lens.

5.2 Imaging device for a wavelength of 4 μm

A first imaging device was designed for a wavelength of $\lambda = 4$ μm, using the geometry and set-up shown in Figure 5.1. The simulation was done for silicon pillars placed on a sapphire substrate, using the transmitted phase information $\phi(d/\Lambda)$ extracted from Figure 4.4b.

Transmission into higher diffraction orders and the excitation of lateral modes investigated in Sections 4.3.4 and 4.3.5 were expected to worsen the focusing behavior of the lens. Another possible cause of defocussing could be the change of the transmitted phase function for increased incidence angles in Figure 4.10 and 4.11. In addition, the Petzval curvature of a lens designed according to Equation 2.1, shifts the focus out of a planar focal plane array for increased incidence angles [12]. To optimize the quality of the focal spot for high incidence angles and keep it in the desired focal plane, the focal length in Equation 2.1 was modified radially with an empirical quadratic correction

$$f(r) = a_1 + a_2 r + a_3 r^2. \tag{5.1}$$

The results of FEM simulations presented below show, that with this correction, imaging with a field of view larger than 120° should be possible with a transmissive sub-wavelength grating lens.

5.2.1 Displacement of the focal spot for off-axis incidence

Figure 5.2 shows the magnitude of the Poynting vector for an imaging device with design wavelength $\lambda = 4$ μm and an incidence angle of $\alpha = 60°$. The simulation was done for TE polarized light, corresponding to a polarization filter in the aperture plane, to avoid the excitation of lateral modes with rather broad resonance observed in Section 4.3.5. For the empirical correction according to Equation 5.1, parameters $a_1 = 270$ μm, $a_2 = -0.065$ and $a_3 = -0.00065$ μm^{-1} were used. It can be seen in Figure 5.2, that with this correction the focal spot is centered in a planar focal plane for an incidence angle of $\alpha = 60°$. The simulation was then rerun for incidence angles from 0° to 60° with a step size of 5°. Figure 5.3a shows the normalized magnitude of the Poynting vector normal component in the focal plane for different incidence angles with a step size of 10°. It was observed, that the peak height is reduced for larger incidence angles to about half of the value for 0° and there are distinct side-peaks for all focal spots. Those issues still have to be addressed. However, compared to reports of severe corruption of the focal spot for incidence angles larger than 10° for other sub-wavelength grating designs [11], the results in Figure 5.3a are an improvement. The displacement of the focal spot was extracted from the simulation results and plotted over the sine of the incidence angle α in Figure 5.3b. A linear fit

$$x_{peak}(\alpha) = b_1 + b_2 \sin(\alpha) \tag{5.2}$$

for the particular design gave fit parameters of $b_1 = (-0.04 \pm 0.16)$ μm and $b_2 = (-159.7 \pm 0.3)$ μm, confirming a close to ideal $\sin(\alpha)$ dependence. Errors can be attributed mostly to

the rather coarse mesh and the linear discretization order used to reduce the simulation effort.

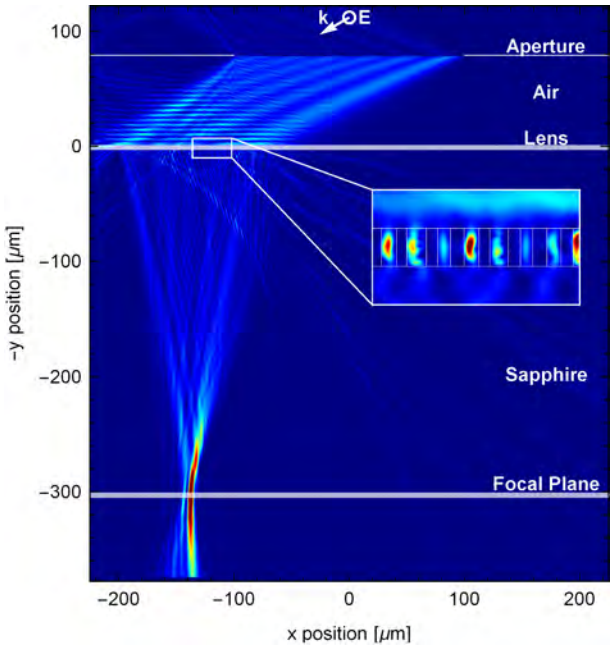

Figure 5.2: Magnitude of the Poynting vector from finite element simulation of the imaging device for a design wavelength of $\lambda = 4$ μm and TE polarized incidence at an angle of $\alpha = 60°$.

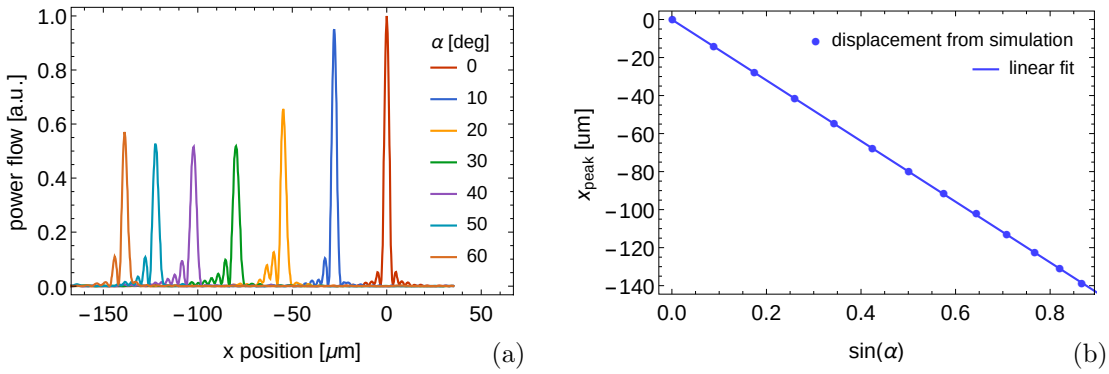

Figure 5.3: Magnitude of the Poynting vector normal component in the focal plane for different incidence angles α (a) and demonstration of $\sin(\alpha)$ dependence of the peak displacement in the focal plane (b).

5.2.2 Chromatic aberration

In order to have an estimation of the theoretical chromatic aberration of the sub-wavelength grating lens, Equation 2.1, which was derived from the Huygens-Fresnel principle, can be rewritten to

$$|f| = \frac{n_{mat}\pi r^2}{\lambda\phi} - \frac{\lambda\phi}{n_{mat}4\pi}. \tag{5.3}$$

For large r the second part can be neglected, resulting in an approximate wavelength dependence of the focal length f

$$f(\lambda) \sim \frac{1}{\lambda}. \tag{5.4}$$

The simulation of the above imaging device for a design wavelength of $\lambda = 4$ μm was run for several wavelengths and TE polarized incidence at an angle of $\alpha = 0°$. Figure 5.4 shows the results indicating considerable chromatic aberration. The cuts along the optical axis in Figure 5.4a and in the focal plane in Figure 5.4b display the magnitude of the Poynting vector normalized with the maximum value obtained for the design wavelength.

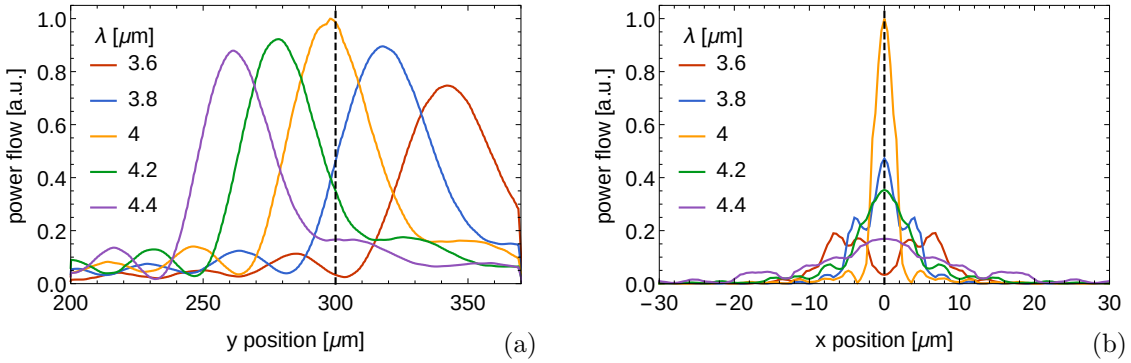

Figure 5.4: Chromatic aberration of an imaging device with a design wavelength of $\lambda = 4$ μm. Cut along the optical axis (a) and in the focal plane (b), showing the normalized magnitude of the Poynting vector for TE polarized incidence at an angle of $\alpha = 0°$ for several wavelengths λ.

The y position of the peaks y_{peak} was then extracted for several wavelengths from the cut along the optical axis and can be found in Figure 5.5. Based on Equation 5.3 the non-linear relation

$$y_{peak}(\lambda) = \frac{c_1}{\lambda} - c_2\lambda \tag{5.5}$$

was used to fit the data. For this particular design of an imaging device, fit parameters of $c_1 = (1387 \pm 6)$ μm^2 and $c_2 = (11.7 \pm 0.4)$ were obtained. The finding that $c_1 \gg c_2$ confirms the approximate chromatic dispersion relation in Equation 5.4. The pronounced chromatic aberration of diffractive optical elements in general [7] and also of the sub-wavelength grating lens in particular, can be a reason to dismiss such a design for broadband imaging.

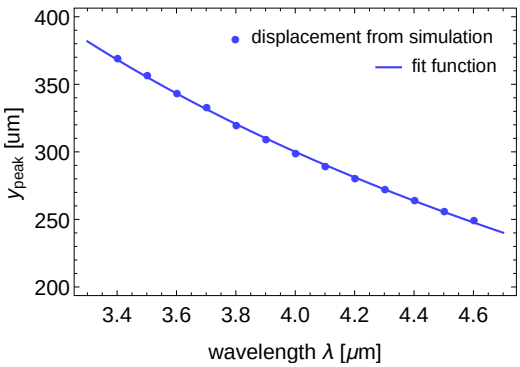

Figure 5.5: Displacement of the focal spot along the optical axis for several wavelengths. The peak position was extracted from Poynting vector magnitude along the optical axis for TE polarized incidence at an angle of $\alpha = 0°$. Equation 5.5 was used to fit the extracted data.

5.2.3 Sensitivity analysis of the focusing performance

For the production of an imaging device incorporating a sub-wavelength grating lens, a sensitivity analysis of the performance on the accuracy of the fabricated grating pillars is highly important. Therefore, simulations were run with pillar height h and diameter d differing from the design values. Figure 5.6 shows the resulting normalized magnitude of the Poynting vector for cuts along the optical axis and in the focal plane. Surprisingly, it was observed, that an increased height of $h = 2.8$ μm can even improve the quality of the focal spot, compared to using $h = 2.6$ μm derived in Section 4.3. For a height of $h = 2.4$ μm and the diameters $d(r)$ of the pillars differing by $|\delta| = 0.06$ μm from their respective design values, the magnitude of the Poynting vector in the center of the focal spot is reduced to about 60% of the value obtained for the original design.

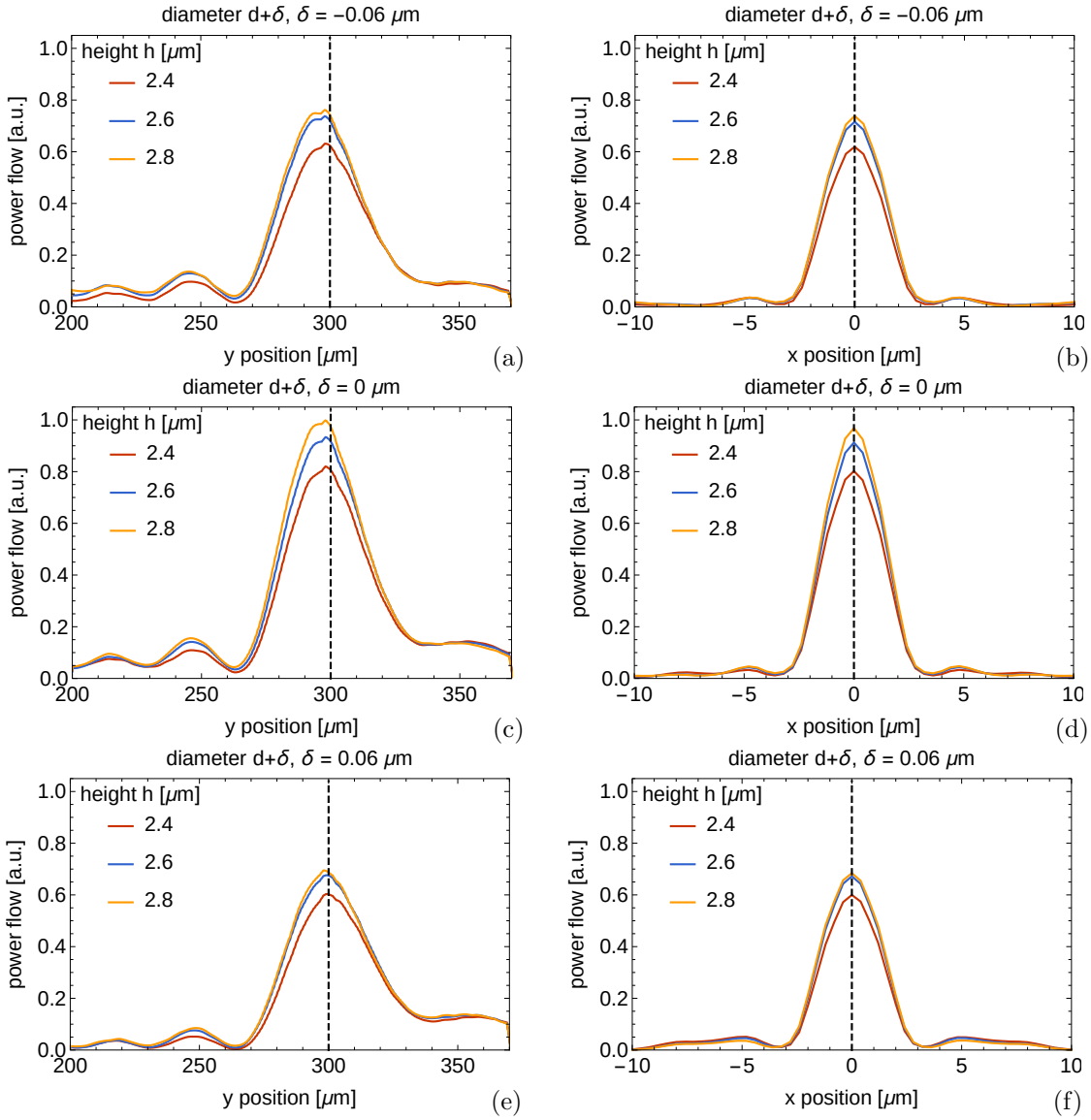

Figure 5.6: Sensitivity analysis of the focusing performance of the imaging device. The magnitude of the pointing vector was normalized with the maximum value for the design wavelength of $\lambda = 4$ μm. Cuts along the optical axis in (a),(c) and (e), as well as in the focal plane in (b),(d) and (f), allow for the comparison of the quality of the focal spot for different heights h of the grating pillars and diameters $d(r)$ differing by δ from their respective design values.

5.2.4 Difference between the TE and the TM polarization

To further investigate the implications of scattering into higher diffraction orders and the excitation of lateral modes observed in Sections 4.3.4 and 4.3.5, the imaging device was also simulated with TM polarized incidence. Figure 5.7 shows the normalized magnitude of the Poynting vector for TE and TM polarized incidence at different angles α. The curves for the TE polarization are plotted in pale colors. As expected, there is no difference for an incidence angle of $\alpha = 0°$, endorsing the validity of the simulation set-up. Also, for incidence angles up to $\alpha = 50°$, the heights of the peaks for TM polarization are only slightly smaller than for the TE polarization. This indicates, that the excitation of lateral modes and scattering into higher diffraction orders have similar effect for the TE and the TM polarization. However, for an incidence angle of 60°, the focal spot for the TM polarization has only half the height compared to the TE polarization. The cause for this was increased scattering off the edge of the sub-wavelength grating lens for TM polarized incidence.

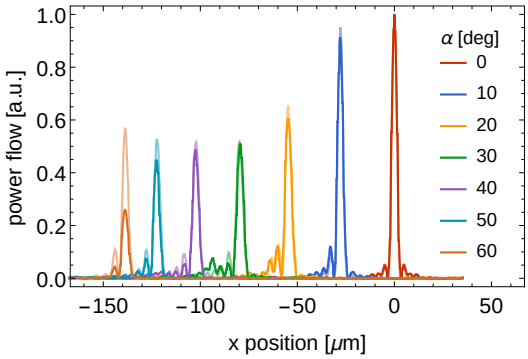

Figure 5.7: Comparison of the imaging performance for the TE and the TM polarization at the design wavelength of $\lambda = 4$ μm. The pale curves show the normalized magnitude of the Poynting vector for TE polarized incidence. The curves with dark colors are for TM polarization.

5.2.5 Gaussian Apodization

The large side-peaks observed in Figure 5.3a and 5.7 diminish the quality of the imaging device. Apodization [12] in the aperture plane is a convenient way to reduce the height of unwanted side-peaks. By using a Gaussian opening function with a standard deviation σ instead of a step function with width a as the port boundary condition, the results presented in Figure 5.8 were obtained.

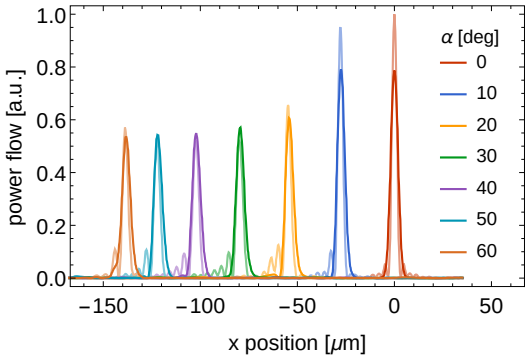

Figure 5.8: Effect of Gaussian apodization in the aperture plane with a standard deviation of $\sigma = 40$ μm. The curves with pale colors show the normalized magnitude of the Poynting vector for TE polarized incidence at several angles α and a conventional aperture. Results for Gaussian apodization are plotted in dark colors.

The curves with pale colors show the normalized magnitude of the Poynting vector for TE polarized incidence and a conventional aperture. Results for Gaussian apodization, plotted in dark colors, show a slight broadening of the central peaks and efficient reduction of the side-peaks.

5.3 Imaging device for a wavelength of 10 μm

An imaging device was also designed for a wavelength of 10 μm, using the transmitted phase information of design A from Figure 4.12b. Similar to the approach presented above, Equation 2.8 was modified radially with the empirical correction in Equation 5.1. Also, instead of Equation 2.7

$$r'_{emp} = \frac{f - t}{r} \tag{5.6}$$

was used. The substrate had a thickness of $t = 100$ μm and the focal length was determined by the parameters $a_1 = 610$ μm, $a_2 = -0.09$ μm and $a_3 = -0.0002$ μm. Gaussian apodization with a standard deviation of $\sigma = 90$ μm was used in the aperture plane to reduce the height of unwanted side-peaks. It can be seen in Figure 5.9 that a focal spot was produced in a distance of approximately 550 μm from the lens plane.

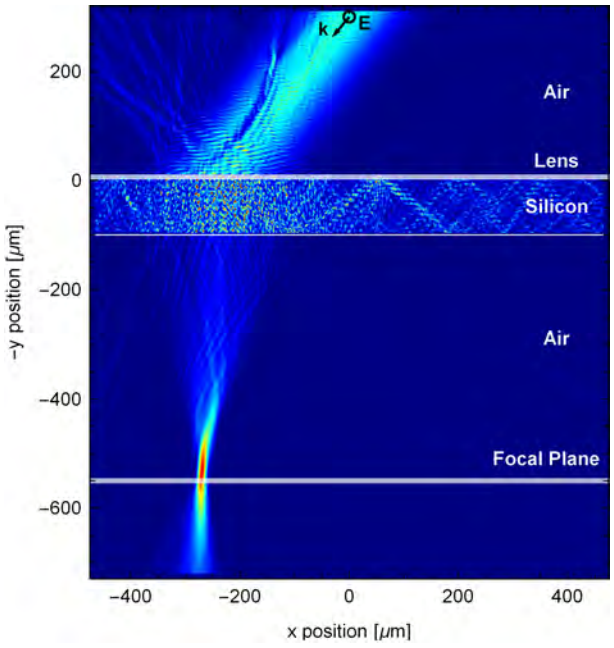

Figure 5.9: Magnitude of the Poynting vector from finite element simulation of the imaging device for a design wavelength of $\lambda = 10$ μm and TE polarized incidence at an angle of $\alpha = 40°$.

The simulation was run for incidence angles from 0° to 50° with a step size of 5°. Figure 5.10a shows the normalized Poynting vector normal component in the focal plane for different incidence angles with a step size of 10°. It was observed that the peak height was reduced for larger incidence angles, but did not drop below 60% of the value observed for 0°. The displacement of the focal spots was extracted from the simulation results and plotted over the sine of the incidence angle α in Figure 5.10b. A linear fit according to Equation 5.2 for this particular design gave fit parameters of $b_1 = (-1.6 \pm 0.5)$ μm and $b_2 = (-418 \pm 1)$ μm, confirming a close to ideal $\sin(\alpha)$ dependence. Again, errors can be attributed mostly to the rather course mesh and the linear discretization used to reduce the simulation effort.

The simulation was then run for several wavelengths from 9 μm to 11 μm and TE polarized normal incidence, to investigate chromatic aberrations. The cuts along the optical axis in Figure 5.11a and in the focal plane located 550 μm from the lens plane in Figure 5.11b display the magnitude of the Poynting vector normalized with the maximum value obtained for the design wavelength.

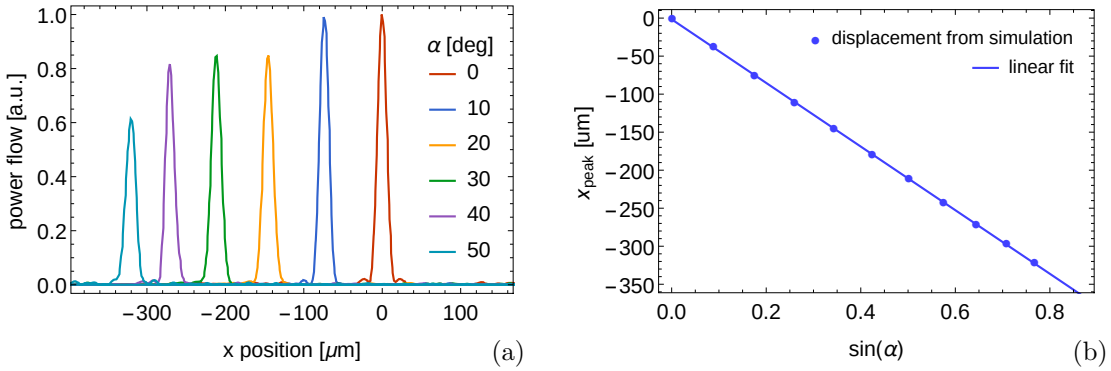

Figure 5.10: Magnitude of the Poynting vector normal component in the focal plane for different incidence angles (a) and demonstration of $\sin(\alpha)$ dependence of the peak displacement in the focal plane on the incidence angle α (b).

Interestingly, the peak height observed for wavelengths other than 10 μm can be larger. This was not observed for the imaging device for a wavelength of 4 μm presented above. Reasons for this might be interference effects due to reflection at the back plane of the substrate and the assumption of infinite coherence length in the simulation.

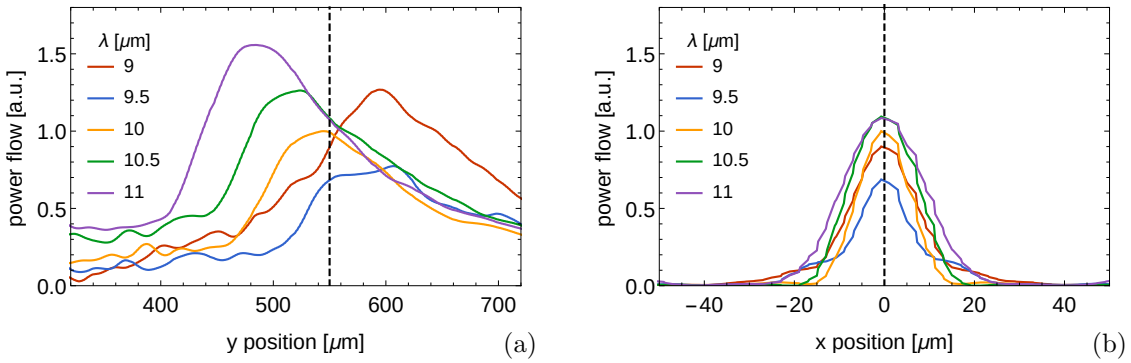

Figure 5.11: Chromatic aberration of an imaging device with a design wavelength of $\lambda = 10$ μm. Cut along the optical axis (a) and in the focal plane (b), showing the normalized magnitude of the Poynting vector for TE polarized incidence at an angle of $\alpha = 0°$ for several wavelengths λ.

5.4 Lens simulations for comparison with experimental results

More FEM wave-optics simulations of full lenses were done for comparison with the experimental results in Section 6.3. Due to limitations of computational resources, it was only possible to simulate the lenses with a diameter of 1 mm and a focal length of 750 μm for wavelengths from 8-12 μm. Besides sub-wavelength grating lenses of design A and B, introduced in Section 4.4, also a conventional Fresnel zone plate [12] was simulated.

5.4.1 Sub-wavelength grating lens of design A and B

The geometry used for the lens simulations was similar to the one shown in Figure 3.5. Cylindrical silicon pillars were placed on a silicon substrate with a thickness of $t = 200$ μm. Equation 2.8 was used to find the phase function for a lens with a focal length of $f = 750$ μm. Figure 5.12 shows the magnitude of the Poynting vector from a simulation of the lens using design A and a wavelength of $\lambda = 10$ μm.

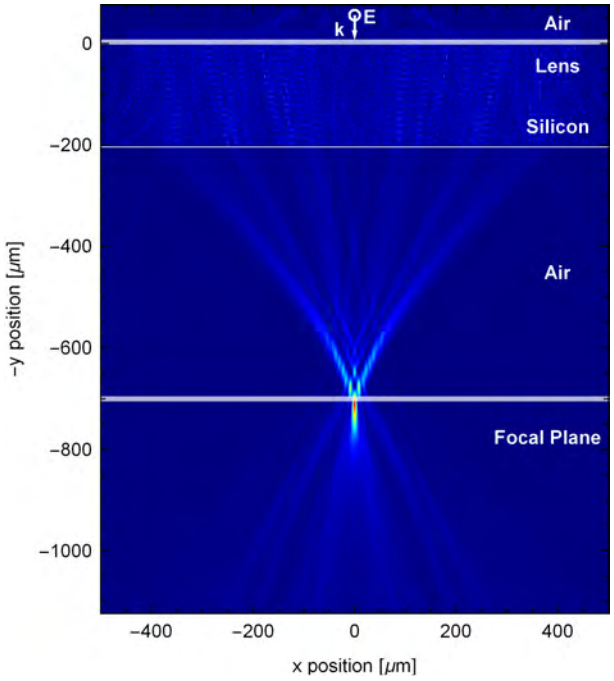

Figure 5.12: Magnitude of the Poynting vector from finite element simulation of the sub-wavelength grating lens using design A for TE polarized incidence with a wavelength of $\lambda = 10$ μm.

FEM simulations were run for nine wavelengths from 8-12 μm. The Poynting vector along the optical axis and in the focal plane was added up to get an estimation for the focal spot. Figure 5.13 shows the respective plots for the lens using design A, the results for design B are in Figure 5.14.

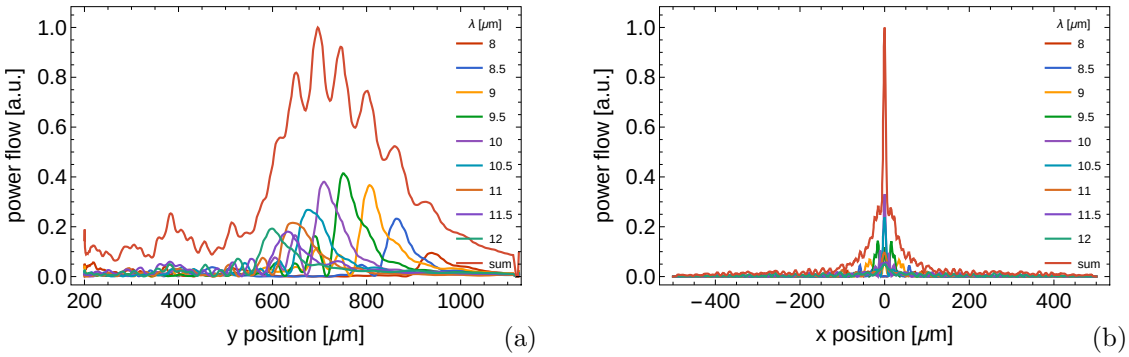

Figure 5.13: Chromatic aberration of a lens for a wavelength of $\lambda = 10$ μm using design A. Cut along the optical axis (a) and in the focal plane (b), showing the normalized magnitude of the Poynting vector for TE polarized normal incidence for wavelengths from 8-12 μm.

The pointing vector magnitude was normalized with the maximum value observed for the sum. Obviously the ripples observed in Figure 5.13 and in Figure 5.14 are an artificial feature, resulting from the finite number of wavelengths used for sum. Adding the results for more wavelengths would smoothen the shape of the focal spot.

The effective focal distance for a broadband source with wavelengths from 8-12 μm was observed to be $f = 700$ μm, rather than the design value of 750 μm. Thus, the cuts in the focal plane in Figure 5.13b and 5.14b are at a y-position of 700 μm. For future sub-wavelength grating lenses a more accurate focal length could be achieved by using an additional optimization routine instead of Equation 2.8.

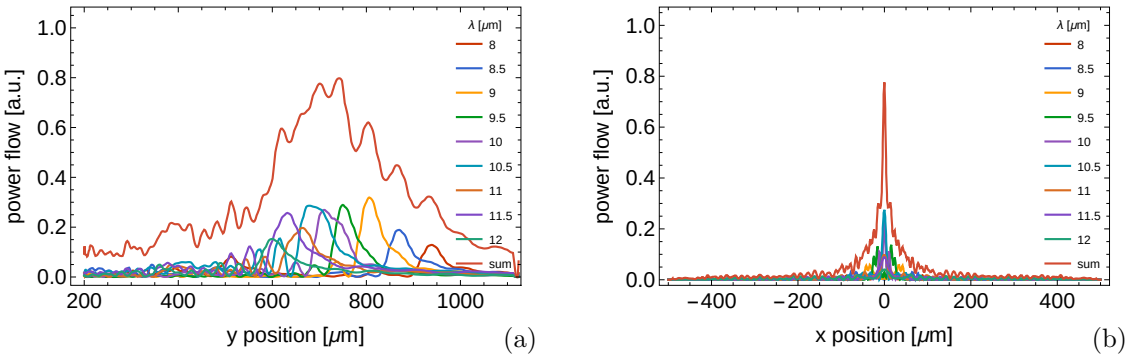

Figure 5.14: Chromatic aberration of a lens for a wavelength of $\lambda = 10$ μm using design B. Cut along the optical axis (a) and in the focal plane (b), showing the normalized magnitude of the Poynting vector for TE polarized normal incidence at for wavelengths from 8-12 μm.

5.4.2 Fresnel Zone Plate

For the simulation of the Fresnel zone plate, a two-dimensional geometry was used. Designed as a phase zone plate, it consisted of 2 μm deep groves etched into silicon. The zone plate had a diameter of 1 mm and a focal length of $f = 720$ μm for a wavelength of 10 μm. Contrary to the sub-wavelength grating lenses, the thickness of the wafer was 650 μm. Figure 5.15 shows the Poynting vector magnitude for cuts along the optical axis and in the focal plane of the zone plate.

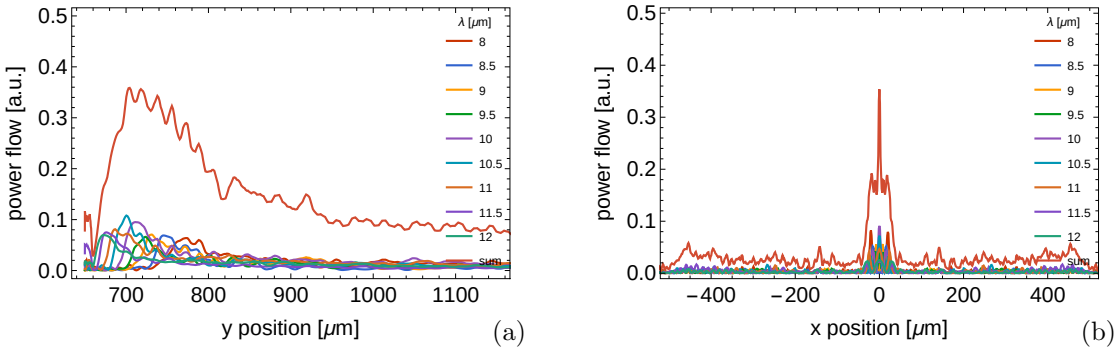

Figure 5.15: Chromatic aberration of a Fresnel zone plate with a focal length of 720 μm for a wavelength of 10 μm. Cut along the optical axis (a) and in the focal plane (b), showing the normalized magnitude of the Poynting vector for TE polarized normal incidence for wavelengths from 8-12 μm.

The incident power used in the simulation of the zone plate was matched to the three-dimensional simulations of the sub-wavelength grating lenses for comparability. The Poynting vector magnitude for the zone plate in Figure 5.15 was also normalized with

the maximum value found for the sum of the Poynting vector magnitudes for the sub-wavelength grating lenses.

5.4.3 Comparison of the simulated lenses

Figure 5.16 compares the quality of the focal spot of sub-wavelength grating lenses using design A and B to the zone plate for illumination with a broadband source (8-12 μm). As expected from the transmission behavior in Table 4.1, the lens using design A, with a grating pitch of $\Lambda = 4.5$ μm, shows a slightly better performance than the lens using design B ($\Lambda = 5$ μm). Both sub-wavelength grating lenses show significantly higher power flow in the focal spot than the Fresnel zone plate. One interpretation for this observation would be, that the sub-wavelength grating reshapes the incident wavefront more accurately. Another factor could be the increased internal reflection at the back-plane of the wafer for the zone plate, due to the larger substrate thickness.

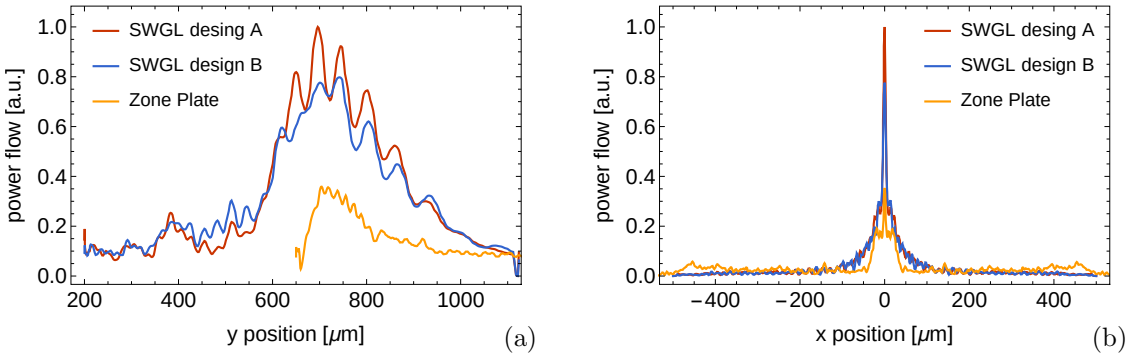

Figure 5.16: Comparison of the simulated focal spot of sub-wavelength grating lenses of design A and B to a Fresnel zone plate. Cuts along the optical axis (a) and in the focal plane (b) show the normalized sum of the Poynting vector magnitude for wavelengths from 8-12 μm.

5.4.4 Estimation of the focusing efficiency

To estimate the focusing efficiency of the lenses for the range of 8-12 μm, the Poynting vectors for single wavelengths were integrated along the boundaries of the simulation geometry. The focusing efficiency was then calculated as the ratio of power flow through a 40 μm wide part around the focal spot to the total incident power. Averaging the values for five wavelengths from 8-12 μm gave a focusing efficiency of 13% for the sub-wavelength grating lens using design A.

6 EXPERIMENTAL VERIFICATION

To verify that the sub-wavelength grating lens designs indeed work, a measurement set-up was built. Several samples with silicon pillars on a silicon substrate were produced using UV lithography and deep reactive ion etching (DRIE). A distinct focal spot was observed for the sample lenses, using a broadband IR source. The performance of the sub-wavelength grating lens designs was compared to the results from simulation and also to a lens with a conventional Fresnel zone plate design. A more in-depth characterization of the focal spot was not possible, due to limitations of the measurement set-up.

6.1 Measurement set-up for IR lens characterization

For the experimental verification of the IR lens designs, a dedicated measurement set-up was needed. One key requirement was, that it should provide a reliable characterization of the width of the focal spot in the desired image plane. Also, an extension to off-axis incidence should be possible.

The conventional solution would be to use a microscope style set-up sketched in Figure 6.1, consisting of a collimated IR source, an objective lens, a tube lens and an IR camera, similar to the set-up described in [4]. This would have the advantage of quick image acquisition. The magnification of the microscope arrangement can be found by imaging a calibration sample, the resolution of such a set-up is limited by the resolution of the IR camera and the magnification of the lens system. For an accurate characterization of the investigated lens, the point transfer functions of objective and tube lens have to be taken into account. It is however difficult to characterize the back focal length with a microscope style set-up. In addition to a large numerical aperture of the objective lens, which is needed to reduce the focal depth and therefore increase the resolution in direction of the optical axis, some kind of reference structure would be needed to identify the back plane of the lens under investigation.

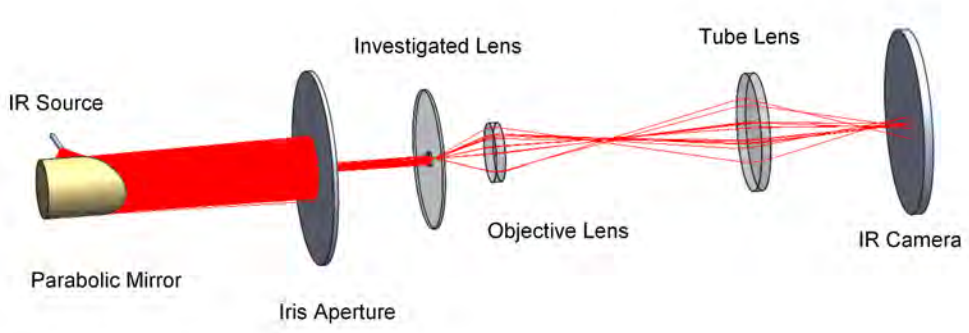

Figure 6.1: Schematic of a microscope style set-up for the characterization of the focal spot of an IR lens. Rays resulting from a ray-tracing simulation with APEX are visualized as red lines. The surface of the parabolic mirror was perfectly reflecting, the surfaces of the iris aperture and the IR camera were perfectly absorbing. For the investigated lens, the objective lens and the tube lens the surfaces were simulated as perfectly transmitting.

6.1.1 Knife-edge measurement set-up

A knife-edge based measurement set-up has the advantage, that sub-wavelength resolved characterization of the focal spot is possible without any further imaging optics [23]. The measurement principle relies on a knife being moved in the back focal plane of the

investigated lens and thereby casting a shadow on a detector. A detector with infinite opening angle collects an intensity I_D depending on the position x_k of the knife edge [12]

$$I_D(x_k) = \frac{c\epsilon_0}{2} \int_{-\infty}^{\infty} \int_{-\infty}^{x_k} |E(x,y,z)|^2 \mathrm{d}z\mathrm{d}x, \tag{6.1}$$

where E is the magnitude of the electric field, c is the speed of light in vacuum and ϵ_0 is the vacuum permittivity. By numerically differentiating the intensity at the detector $I_D(x_k)$, the profile of the focal spot $I_F(x,y)$ can be obtained

$$I_F(x,y) = \left| \frac{\partial I_D}{\partial x_k} \right|_{x_k=x} = \frac{c\epsilon_0}{2} \int_{-\infty}^{\infty} |E(x,y,z)|^2 \mathrm{d}z. \tag{6.2}$$

The need for numerical differentiation impairs the signal to noise ratio (SNR) of the measurement method. An improved knife-edge based measurement method uses an oscillating knife-edge driven by a piezo-element and a lock-in amplifier to detect the signal [24]. By using this technique, the slope of $I_D(x_k)$ is measured directly, without the need of numerical differentiation.

For the experimental verification of the IR lens designs, a basic knife-edge based measurement set-up was designed at first. Gold coated mirrors were used instead of IR lenses, to reduce the chromatic aberration of the measurement set-up and facilitate the alignment of the set-up with a low-power visible range laser diode. Figure 6.2 shows the schematic, with the following components from the left to the right, in the main direction of light propagation. A thermal IR emitter was located in the focal point of a gold-coated 90° off-axis parabolic mirror ($f_p = 25.4$ mm), collimating the light. For the alignment of the set-up the thermal emitter was replaced by a red low-power laser diode. An adjustable iris aperture blocked light, so only the lens under investigation was illuminated. A gold-coated spherical mirror ($f_s = 56.5$ mm) was placed at a distance of two times its focal length from the focal point of the investigated lens, to collect light from the lens and facilitate movement of the knife-edge along the optical axis. Light reflected by the spherical mirror was then focused on the mercury cadmium telluride (MCT) detector, located at a distance of two times the focal length f_s from the spherical mirror.

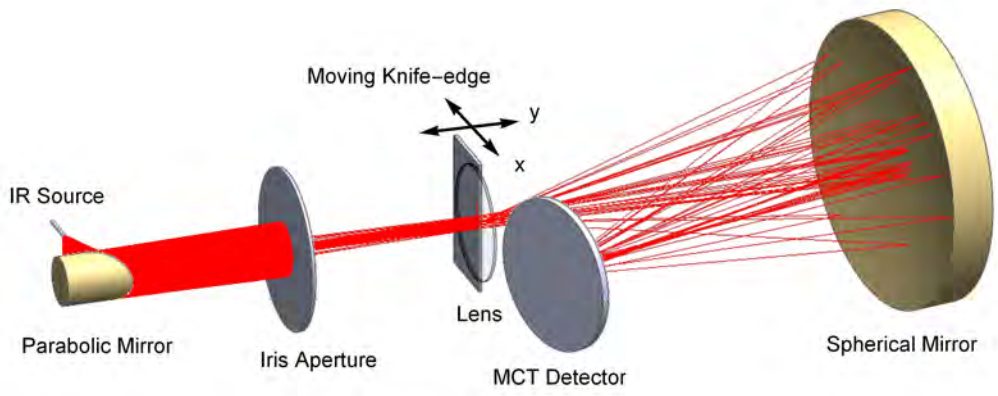

Figure 6.2: Schematic of a knife-edge based measurement set-up for the characterization of the focal spot of IR lenses. Rays resulting from a ray-tracing simulation with APEX are visualized as red lines. The surfaces of the gold-coated mirrors were simulated as perfectly reflecting, the surfaces of the iris aperure, the knife-edge and the mercury cadmium telluride (MCT) detector as perfectly absorbing.

To confirm the viability of the devised set-up, ray-tracing simulations were performed with APEX, an add-in for Solid Works. Rays resulting from these simulations are also

visualized in Figure 6.2. For the simulation the surfaces of the gold-coated mirrors were set as perfectly reflecting coatings. The surfaces of iris aperture, knife-edge and detector were set as perfectly absorbing coatings and a ZnSe lens with a diameter of 2 mm and a focal length of 2 mm was used for the lens under investigation. A diameter of 2 mm was also used for the iris aperture. A circular disk with a diameter of 0.5 mm was used for the IR emitter. The rays had a wavelength of 10.6 μm and an angular distribution according to the data-sheet of the INTEX 17-0900 emitter.

In a first ray-tracing simulation the viability of the simple collimation set-up, consisting only of the parabolic mirror and the iris aperture, was investigated. Therefore an additional absorber was placed in the focal plane of the lens under investigation, instead of the knife edge. The simulation was done for 5×10^6 rays and subsequently the irradiance on the absorber in the focal plane was calculated. The result shown in Figure 6.3 was averaged radially and normalized with the maximum intensity.

For comparison, Figure 6.3 shows also the diffraction limited spot size of a lens with a focal length of 2 mm and an aperture diameter of 0.8 mm. The Airy pattern $I_A(r)$ of a lens with focal length f and an aperture diameter a was calculated according to [12]

$$I_A(r) = 2\left(J_1\left(\frac{\pi a r}{\lambda f}\right)\frac{\lambda f}{\pi a r}\right)^2, \tag{6.3}$$

where λ is the wavelength and J_1 is the Bessel function of the first kind. For easier comparison, the Airy pattern was rescaled, so the peak would also correspond to an irradiance of 1. Figure 6.3 shows, that the spot from the ray tracing simulation and the diffraction limited spot have approximately the same width. This means, that for the investigation of a lens with a focal length of 2 mm and an aperture diameter below 0.8 mm, the collimation of the IR source in the measurement set-up is sufficient.

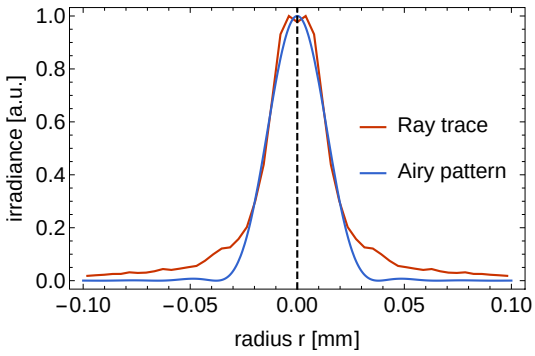

Figure 6.3: Comparison of the spot size from a ray-tracing simulation of a lens with a focal length of 2 mm to the diffraction limited spot size with an aperture diameter of 0.8 mm.

Additionally, also the knife-edge measurement method was simulated by ray-tracing. To reduce the simulation effort, a light source emitting parallel light was placed in the opening of the iris aperture. This way, the simulations could be done with only 2×10^5 rays for each position of the knife edge. The knife-edge was moved a total distance of 60 μm, while at 61 equally spaced measurement points the total irradiance I_D on the MCT detector was collected. Numerical differentiation of the $I_D(x_k)$ data obtained from the simulation was done by central difference, to accurately represent the peak position. For comparison with the simulated knife-edge data another simulation was run with 5×10^6 rays and an absorber in the focal plane of the investigated lens, instead of the knife. The irradiance on the absorber inside a quadratic window with a side length of 60 μm was averaged

radially and also along the z-direction for comparison with the knife-edge data. Figure 6.4 compares the focal spot obtained with the simulated knife-edge measurement and from the absorber in the focal plane. The irradiance data was normalized with the respective maximum value, to allow for better comparability.

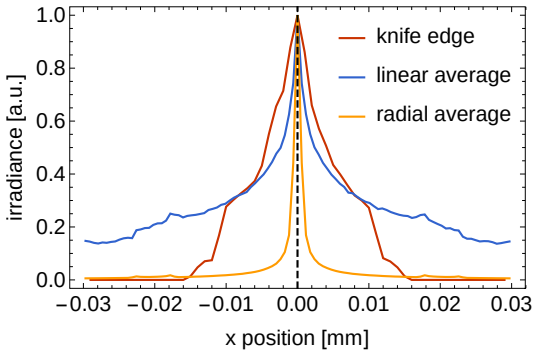

Figure 6.4: Comparison of the spot-size obtained by a simulated knife-edge measurement to the radially averaged spot size obtained by a conventional ray-tracing simulation. The linear average is along a length of 60 μm in z-direction, centered around the focal spot. This corresponds to the data one would expect to collect with a knife-edge measurement.

It was observed that according to the simulation, the knife-edge measurement can accurately determine the position of the focal spot. However, due to the fact that the measurement technique integrates in z-direction and the limited opening angle of the spherical mirror [23], the width of the focal spot was overestimated. These findings should be kept in mind, when interpreting results from an actual knife-edge measurement. Also note that the ray-tracing simulations do not account for diffraction and the focal spots in Figure 6.4 are way below the diffraction limit shown in Figure 6.3. Nevertheless, the ray-tracing simulations showed that the proposed set-up should work in principal, if a sufficient signal to noise ratio (SNR) is achieved.

The set-up was then built using a liquid nitrogen cooled MCT detector (EOS MCT14-020-E-LN6) and a thermal IR source (Laser Components DLS-200X0808), modulated with a frequency of 5 Hz. The modulation frequency was kept low, to have a large modulation depth of the IR source and therefore a large signal from the AC coupled MCT detector. However, eventually it was found that with this basic set-up, the necessary SNR for a knife-edge based measurement cannot be achieved.

6.1.2 Scanning slit measurement

As a back-up solution, that could be built using existing equipment, a scanning slit measurement system was devised. This method has the advantage that no numerical differentiation is needed, which improves the SNR compared to a classical knife-edge based measurement. However, the resolution of the measurement method is limited by the width of the slit. The intensity collected at the detector I_D can ideally be described as the convolution of the focal spot profile with the slit opening function O_s [12]

$$I_D(x,y) = \frac{c\epsilon_0}{2} \int_{-\infty}^{\infty} \int_{-\infty}^{\infty} O_s(\chi)\, |E(x-\chi,y,z)|^2 \mathrm{d}z\mathrm{d}\chi, \tag{6.4}$$

where E is the magnitude of the electric field, c is the speed of light in vacuum, ϵ_0 is the vacuum permittivity and χ is a dummy variable for the convolution.

Figure 6.5 shows the schematic of the slit-based measurement set-up and rays from a ray-tracing simulation with APEX. The set-up consisted of a thermal IR source (Laser Components DLS-200X0808) located in the focal point of a gold-coated 90° off-axis parabolic mirror (Thorlabs MPD127127-90-M01, $f_p = 25.4$ mm). An adjustable iris aperture (Thorlabs SM1D12CZ) blocked part of the collimated light, so only the lens under investigation would be illuminated. A metal slit with a width of 125 μm was placed in front of the opening of the liquid nitrogen cooled MCT detector (EOS MCT14-020-E-LN6). The detector and the slit were mounted on a x-y stage (Thorlabs LNR50S/M), which was driven by a dedicated control unit (Thorlabs BSC202).

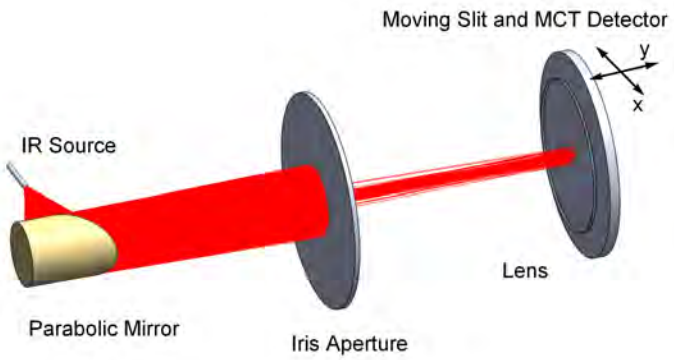

Figure 6.5: Schematic of the scanning slit measurement set-up for the characterization of the focal spot of IR lenses. Rays resulting from a ray-tracing simulation with APEX are visualized as red lines. The surface of the gold-coated parabolic mirror was simulated as perfectly reflecting. The surfaces of iris aperture, slit and detector were simulated as perfectly absorbing.

In addition to the parts shown in Figure 6.5, the set-up also included an optional 8-12 μm bandpass filter, which can be seen in Figure 6.6. Figure 6.7 shows the full bench with the scanning slit measurement set-up.

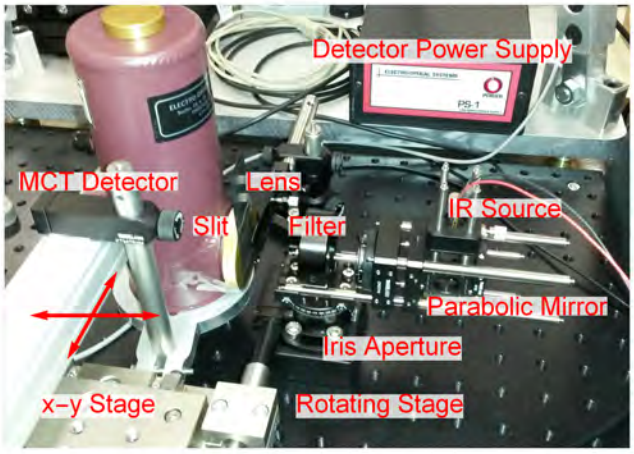

Figure 6.6: Optical part of the scanning slit measurement set-up for the characterization of the focal spot of IR lenses. The thermal IR source was placed in the focal spot of a gold-coated off-axis parabolic mirror with a focal length of $f_p = 25.4$ mm. An adjustable iris aperture was used to block part of the collimated light and illuminate only the lens under investigation. A filter with a passband from 8-12 μm was optionally inserted into the optical path to restrict the investigated wavelength range. A slit with a width of 125 μm and the mercury cadmium telluride (MCT) detector were mounted on a x-y stage and scanned for the measurement.

This includes the frequency generator (Wavetec model 81), which was used as a power supply for the thermal IR source. A sinusoidal signal with a peak-to-peak amplitude of 4 V and a frequency of 5 Hz was used, to allow for an appropriate modulation depth of the IR Source. The MCT detector was powered by a dedicated power supply (EOS PS-1). The MCT detector picked up a signal with a frequency of 10 Hz, which was amplified 10-fold by an internal liquid nitrogen cooled preamplifier. The signal was then fed into a low noise preamplifier on line power (Stanford Research Systems Model SR560) for 50-fold amplification and bandpass filtering around 10 Hz with 6 dB/Oct suppression.

The filtered signal was fed into a digital oscilloscope (Tektronix TDS 2024), which was read out via a GPIB to USB adapter (NI GPIB-USB-HS) by a LabView control program. In the LabView program, additional digital filtering of the signal with 1 % bandwidth was applied and for cases of low SNR, multiple measurements were taken for each position of the slit. The LabView program also controlled the x-y stage (Thorlabs LNR50S/M) via a dedicated control unit (Thorlabs BSC202). To align the optical part of the measurement set-up, the thermal IR source was replaced by red laser diode (Thorlabs L637P5). The source measurement unit (SMU) in Figure 6.7 was used as a power supply for the laser diode.

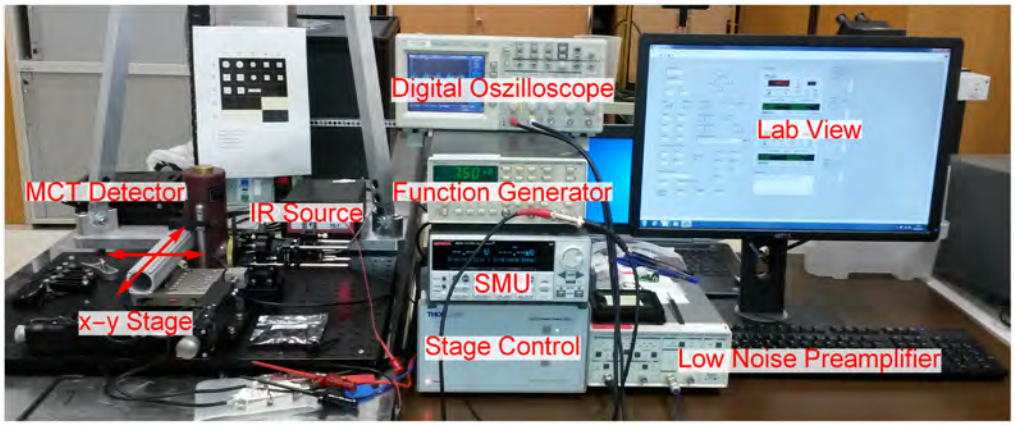

Figure 6.7: Full view of the scanning slit measurement set-up for the characterization of the focal spot of IR lenses. The function generator served as power supply of the thermal IR source, which was modulated at 5 Hz. The mercury cadmium telluride (MCT) detector, which was mounted on a x-y stage, picked up a signal with a frequency of 10 Hz. The signal was filtered and amplified by the low noise preamplifier and fed into a digital oscilloscope, which was connected to a PC. A LabView program was used to digitally filter the signal from the detector and control the x-y stage. A source measurement unit (SMU) was used as the power supply of a red laser diode, which was used to align the optical part of the set-up.

The signal to noise ratio of the scanning slit measurement set-up could be improved in almost the same ways as for the knife-edge based set-up. By using the a chopper in combination with a lock-in amplifier higher modulation frequencies could be achieved, which would enable faster acquisition and also improve the SNR. If the SNR is sufficiently high, the width of the slit can be decreased, improving the spatial resolution of the measurement. Optionally, the scanning slit can be changed to a scanning aperture, which would enable three-dimensional characterization of the focal spot. By using a tunable quantum cascade laser instead of the thermal IR source, chromatic aberrations of the investigated lens could also be quantified. Using a laser source would also significantly increase the signal and therefore improve the SNR.

6.2 Production of the sub-wavelength grating lens

Samples with several sub-wavelength grating lenses, consisting of silicon pillars on a silicon substrate, were produced using conventional lithographic techniques. Two designs with different grating pitch, presented in Section 4.4, were used to find the diameter of the silicon pillars for a transmissive lens. For each design, lenses with different focal length, geometry and shape of the focal spot were produced. The layout of the structures was generated using an open-source GDS Matlab library [25]. Figure 6.8 shows the layout of the twelve different lenses placed on the test-chip, Table 6.1 lists the respective parameters.

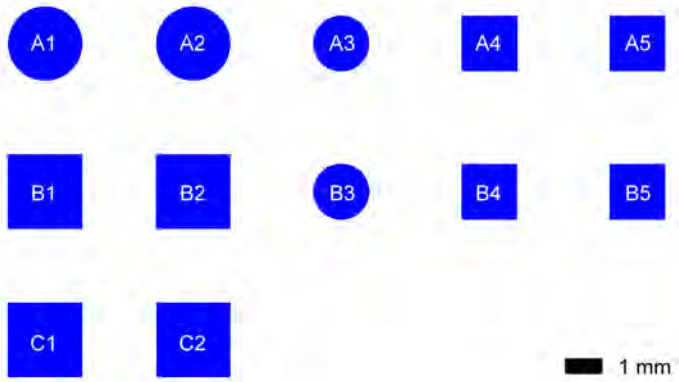

Figure 6.8: Layout of the test-chip with several sub-wavelength grating lens designs. The lenses differ in focal length, geometry, size and also have different shape of the focal spot, as listed in Table 6.1.

Table 6.1: Parameters of the sub-wavelength grating lenses on the test-chip. The size of the lenses means either the diameter or the side length, depending on the geometry. For two different focal lengths f the lenses were designed to either have a point- or line-shaped focus. Design A and B, introduced in Section 4.4, have different grating pitch Λ.

position	f [mm]	focal spot	geometry	size [mm]	design	Λ [μm]
A1	5	point	circle	2	A	4.5
B1	5	point	square	2	A	4.5
C1	5	line	square	2	A	4.5
A2	5	point	circle	2	B	5
B2	5	point	square	2	B	5
C2	5	line	square	2	B	5
A3	0.75	point	circle	1.5	B	5
B3	0.75	point	circle	1.5	A	4.5
A4	0.75	point	square	1.5	B	5
B4	0.75	point	square	1.5	A	4.5
A5	0.75	line	square	1.5	B	5
B5	0.75	line	square	1.5	A	4.5

For the production of the sample lenses polished 100 silicon wafers were first coated with a state of the art positive resist. The lens structure was then exposed with a state of the art semiconductor manufacturing lithography tool and subsequently developed. Deep reactive ion etching (DRIE) was used to produce the silicon pillars from the resist structure. After the etch, the resist was ashed and the wafer thinned and polished to a thickness of 200 μm. The etch depth varied from the center to the edge of a wafer. Two wafers were etched in

total and samples from the center and from the edge, having different height h of the silicon pillars, were investigated. Table 6.2 lists the respective values. The height in sample 1 closely matches the design value of 6.25 μm, the values for sample 2 and 3 are below and above.

Table 6.2: Height of the cylindrical silicon pillars on the etched samples from different parts of the wafers.

sample number	wafer number	cylinder height h [μm]
1	1	6.3 ± 0.1
2	1	6.1 ± 0.1
3	2	6.5 ± 0.1

Figures 6.9-6.11 show optical microscope pictures of the produced sub-wavelength grating lenses. The lens with a focal length of $f = 5$ mm and a diameter of 2 mm in Figure 6.9 has eleven ring-shaped zones, resulting from the modulo 2π division used in the design. Even for the outermost zone its radius is well above the grating pitch. The lens with a focal length of $f = 750$ μm and a diameter of 1.5 mm in Figure 6.10 shows Moiré artifacts, resulting from undersampling. Microscope pictures with increased magnification show, that this effect is not caused by the image acquisition, but inherent to the lens structure. The radius of the outer zones is in the range of the grating pitch, causing the observed Moiré patterns. This undersampling was expected to decrease the focusing efficiency compared to lenses with smaller numerical aperture.

Figure 6.11 shows a lens with a focal length of $f = 750$ μm, designed to focus on a line. This geometry was chosen to allow for better comparability with the wave-optics simulations in Section 5.4. Similar to the lens focusing on a point in Figure 6.10, undersampling can be observed for the outer zones of this lens.

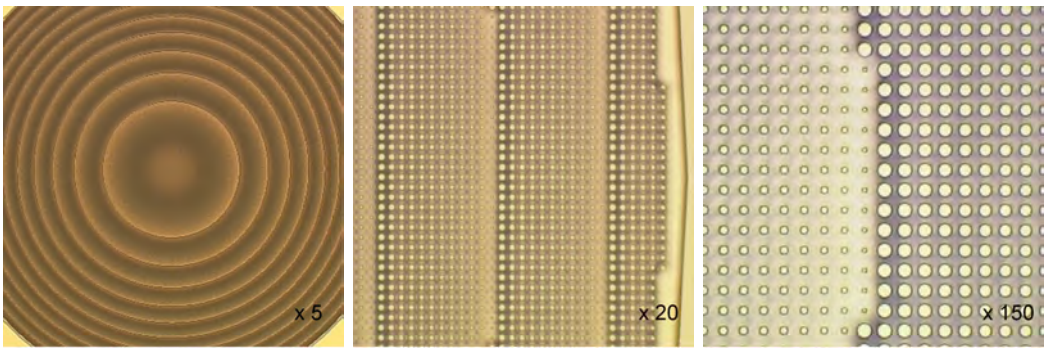

Figure 6.9: Optical microscope pictures of the sub-wavelength grating lens on position A1. The lens was designed for a point-shaped focus at a distance of 5 mm using design A with a grating pitch of 4.5 μm. The number in the right corner shows the used objective magnification.

More production imperfections were observed in the SEM picture in Figure 6.12. The sidewall structure of the silicon pillars, highlighted by charging effects, is characteristic for deep reactive ion etching (DRIE). Also the roughness and elevation of the silicon substrate surface near the cylinders is a result of the etching process. Since DRIE is quite sensitive to the process parameters [26], there is room for optimizations, which could minimize the roughness of the silicon surface and on the cylinder sidewalls. Improving the quality of the etched structures could be a means to increase the focusing efficiency of the sub-wavelength grating lenses.

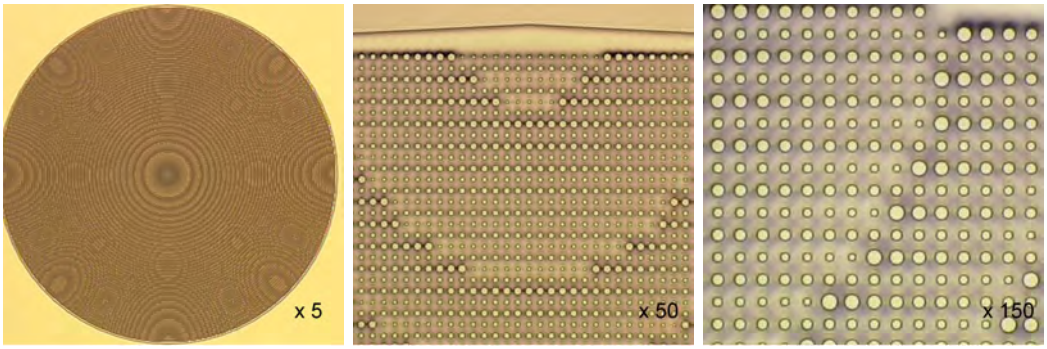

Figure 6.10: Optical microscope pictures of the sub-wavelength grating lens on position A3. The lens was designed for point-shaped focus at a distance of 750 μm using design B with a grating pitch of 5 μm. The number in the right corner shows the used objective magnification.

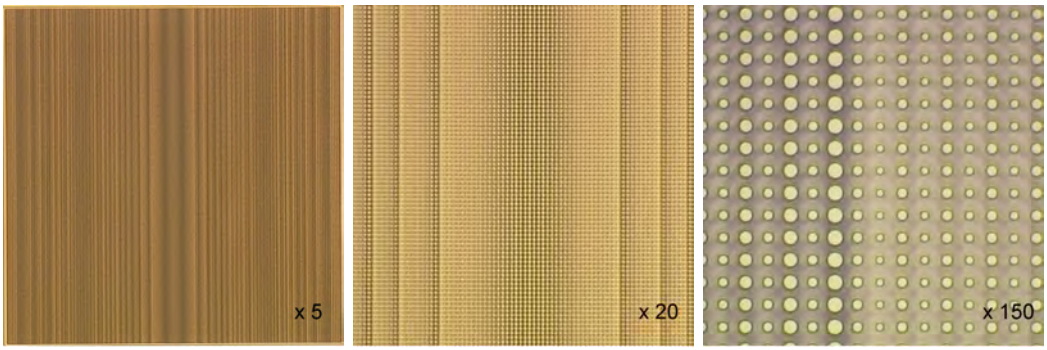

Figure 6.11: Optical microscope pictures of the sub-wavelength grating lens on position A5. The lens was designed for line-shaped focus at a distance of 750 μm using design B with a grating pitch of 5 μm. The number in the right corner shows the used objective magnification.

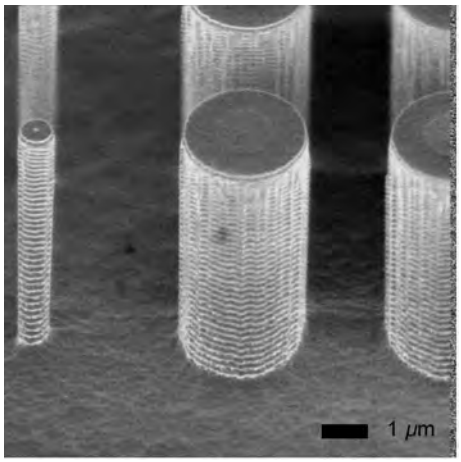

Figure 6.12: SEM picture of a test-structure showing the silicon pillars of the sub-wavelength grating lens in detail. Charging effects highlight the sidewall structure resulting from deep reactive ion etching. Roughness and elevation of the silicon substrate surface near the cylinders is also a result of the etching process.

6.3 Results of the scanning slit measurements

For all the scanning slit measurements the detector signal I_D was measured in arbitrary units, because no reference source was available to calibrate the detector. Also, the main interest of the investigations was qualitative characterization of the focal spots and not absolute irradiance values. To measure the noise floor I_0, the thermal IR source was turned off and an average over 100 measurements gave a value of $I_0 = (1.6 \pm 0.1)$ [a.u.].

The y-position was measured from the back plane of the lens samples, making it necessary to accurately align slit and detector with the sample wafer. In practice this proved to be difficult with the current basic set-up, meaning that the comparison of y-position values from sample to sample is not feasible. Also, a minimum spacing of approximately 100 μm was used to avoid scratching of the wafer surface. To circumvent this inaccuracy of the measurement set-up, comparisons were only made, once the focal spot was located. Another source of error was the alignment of the thermal IR source and iris aperture with the sample lenses. The visible range laser proved to be helpful in this matter, but a better solution would be to lithographically place additional apertures on the sample wafer.

6.3.1 Influence of the bandpass (8-12 μm) filter

Despite having significantly better SNR than the knife-edge measurement set-up, for the lens samples with a focal length of $f = 750$ μm it was not feasible to use a bandpass filter with the scanning slit measurement. The 8-12 μm filter significantly decreased the SNR and increasing the number of measurements per point accordingly would have taken too much time per measurement.

Figure 6.13 compares the focal spot measured with and without the IR bandpass filter for the sub-wavelength grating lens on position B5 of sample 1. It was observed that without the filter, the focal spot moves away from the back plane of the wafer. Previous investigations of the chromatic aberrations in Section 5 predict this behavior. In addition, the large background added without a filter shows that, outside of the 8-12 μm range the focusing performance of the lens is rather poor. The measurements for the plots in Figure 6.13 had a resolution of 71 $\times$ 31 points, quadratic interpolation was used to smoothen the data. With the filter 8 measurements were taken per point, without the filter 3 measurements per point were sufficient.

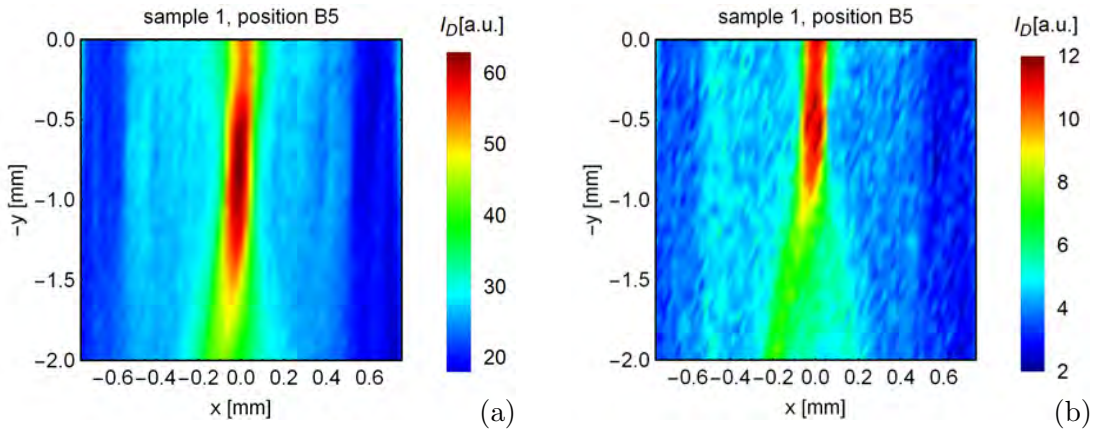

Figure 6.13: Influence of the 8-12 μm bandpass filter on the focal spot measured with the scanning slit method. Without the filter (a) the focal spot is moved away from the back plane of the wafer in accordance with investigations of the chromatic aberrations in Section 5. Using the filter (b) also significantly reduces the background.

6.3.2 Comparison with simulation results

The measurement results for the lens on position B5 of sample 1 were then compared to the simulation results from Section 5.4. This lens uses design A with a focal length of $f = 750$ μm and a has line-shaped focal spot, corresponding to the geometry used in the simulations.

As a first step, the noise floor I_0 was subtracted from detector signal I_D and the resulting signal was normalized with its maximum value. The y-position was offset by 300 μm to account for the minimum spacing of 100 μm between slit and wafer and the wafer thickness of 200 μm. The error of the y-position values was assumed to be 100 μm. The x-position was also offset to center the focal spot. Note that the error-bars of the normalized signal in Figure 6.15 only include statistical errors and disregard any additional errors that could by caused by the misalignment of the illumination part.

To improve the agreement with the scanning slit measurement, the simulations from Section 5.4 were rerun, accounting for the deviation of the cylinder geometry observed in the microscope images. The surface structure of the cylinder sidewalls and the substrate was not included in the simulation. Also, the simple summation of signals from different wavelengths used in Section 5.4 can be improved for comparison with the measurement. Therefore a weighting function was constructed by multiplying the spectral intensity of a blackbody source [12] with the spectral sensitivity of the MCT detector. The temperature value of 700°C for the blackbody was taken the from the data-sheet of the thermal IR source. The pointing vector magnitudes for different wavelengths from the simulation were weighted with this function and subsequently added.

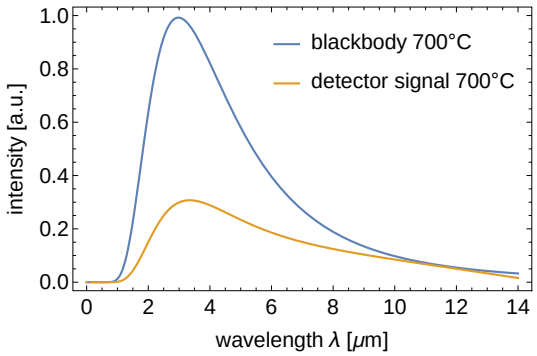

Figure 6.14: Planck's law [12] gave the spectral intensity of a blackbody source at a temperature of 700°C. The expected detector signal used as weighting function was obtained by multiplying the blackbody curve with the spectral sensitivity function of the MCT detector.

The resolution of the scanning slit measurement is limited by the slit opening function. In a last step, the simulation results were modified according to this measurement limitation. Therefore not only the Poynting vector magnitude along the optical axis was used, but the values of 13 cut lines were averaged corresponding to a slit width of 125 μm used in the measurement. The Poynting vector magnitude data in the focal plane was convolved with the slit opening function to obtain the curve labeled "Modified Simulation" in Figure 6.15b. The curves labeled "Simulation" in Figure 6.15 were produced using the simplified approach presented in Section 5.4.

Modifying the simulation, so it more accurately represents the scanning slit measurement, gives better agreement compared to the simplified approach. Especially the observed width of the focal spot in the focal plane is clearly limited by the measurement set-up. While for the width in Figure 6.15b the modified simulation and the measurement show

good agreement, there is some additional background signal that simulation does not predict. This could be caused by a poor extinction ratio of the 8-12 μm filter or by additional scattering due to imperfections of the lithographically produced lens structure. Another explanation for the difference might be the fact that the simulation is for a lens with a diameter of 1 mm, while the measured sample lens has a side length of 1.5 mm. Because of the larger numerical aperture, the sample lens shows under-sampling in the outer area, causing unwanted scattering and thereby more background signal. However, the observation of similar background levels for lenses with smaller numerical aperture contradicts this presumption.

Simulation and measurement results along the optical axis in Figure 6.15a show less agreement. The modified simulation is already closer, but the measured length of the focal spot is still larger than for both predictions. A reason for this might be, that the measure of averaging several line-scans does not accurately reproduce what happens for the measurement. The ripples observed in the curves from the simulation however, are an artifacts resulting from the finite number of simulated wavelengths.

Different spatial and temporal coherence is another more fundamental potential cause for disagreement between measurement and simulation. While infinite coherence length and perfect plane wave incidence is assumed for the simulation, this is of course not the case for the illumination using a thermal IR source in the measurement.

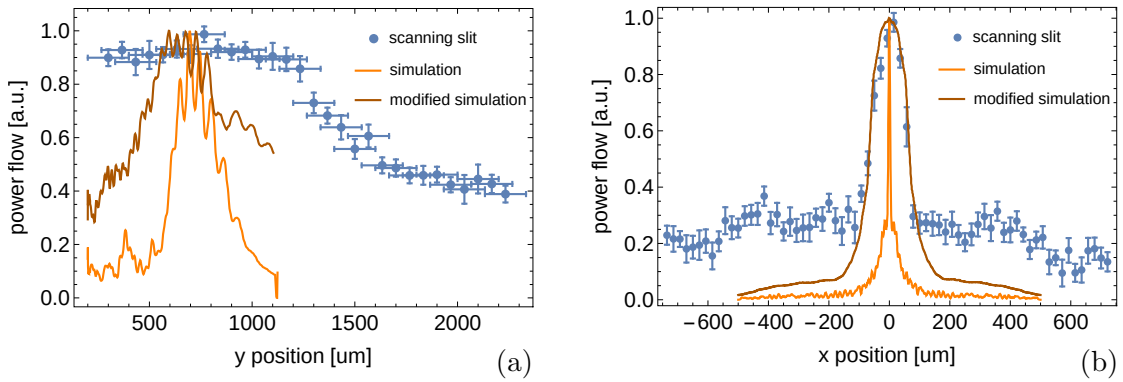

Figure 6.15: Comparison of the scanning slit measurement results to wave-optics simulations. The investigated lens on position B5 of the test-chip had a focal length of $f = 750$ μm and a line-shaped focal spot, corresponding to the geometry used in the simulations.

6.3.3 Sub-wavelength grating lenses with a focal length of 750 μm

The other lenses with a focal length of $f = 750$ μm on sample 1 were measured without the use of a broadband filter. The measurements for the plots in Figure 6.16 had a resolution of 71× 31 points and quadratic interpolation was used to smoothen the data. 3 measurements were taken per point to improve the SNR. The background signal was large, compared to the measurement using the broadband 8-12 μm filter in Figure 6.13b. Nevertheless, a distinct focal spot was observed for all the investigated sample lenses.

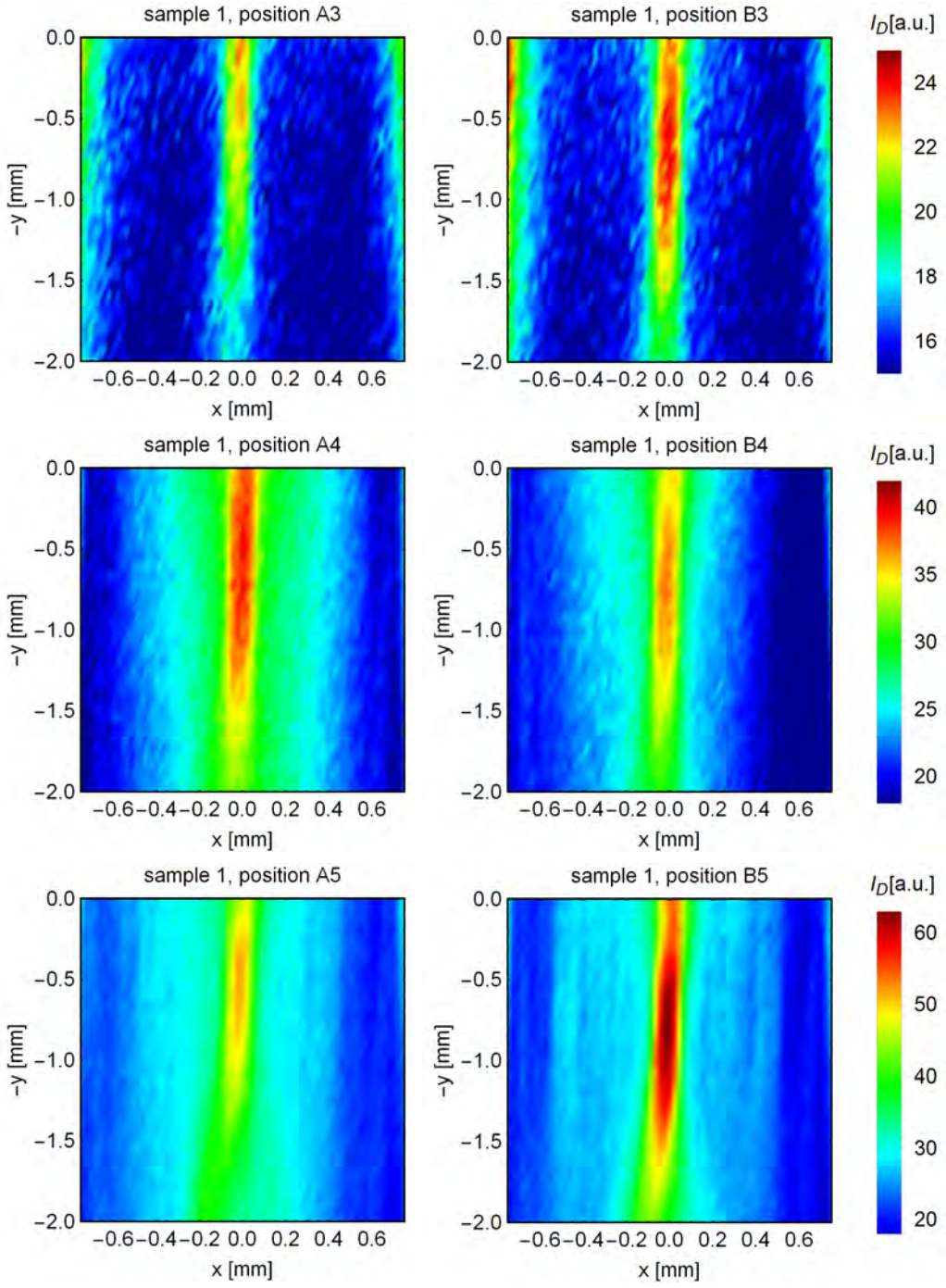

Figure 6.16: Focal spots of sub-wavelength grating lenses with a focal length of $f = 750$ μm, measured with the scanning slit method. The smoothened data had a resolution of 71×31 pixels, the slit had a width of 125 μm and 3 measurements were taken per point to improve the SNR.

6.3.4 Sub-wavelength grating lenses with a focal length of 5 mm

Lenses with a focal length of $f = 5$ mm showed a better focusing performance, so it was possible to use the 8-12 μm filter while only taking one measurement per point. A resolution of 101×51 points was used and quadratic interpolation produced the smoothened plots in Figure 6.17. A clear focal spot could be observed for all investigated sample lenses

and a more detailed comparison of the focal spot for the different lenses is presented next.

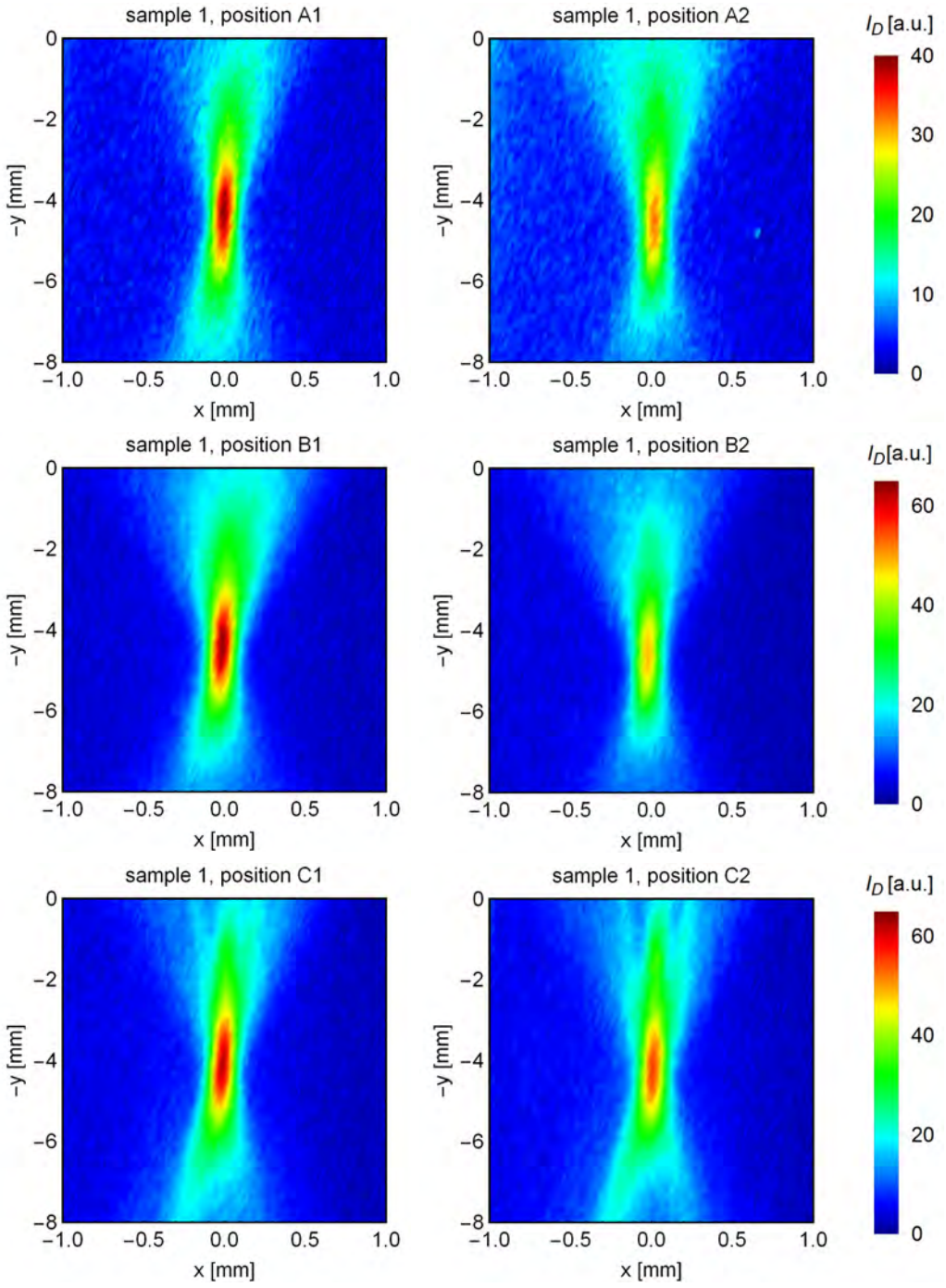

Figure 6.17: Focal spots of sub-wavelength grating lenses with a focal length of $f = 5$ mm, measured with the scanning slit method. The smoothened data had a resolution of 101×51 pixels, the slit had a width of 125 μm and a 8-12 μm filter was used.

6.3.5 Comparison of different lens designs

Simulations in Section 5.4 predict a slightly better performance of the sub-wavelength grating lenses using design A. To be able to compare the results of the measurement

in the focal plane, the detector signal was fit with a Gaussian for the focal spot and a quadratic function for the background

$$I_D(x) = a\, e^{-\frac{(x-x_0)^2}{2\sigma^2}} + b_1 x^2 + b_2 x + b_3. \tag{6.5}$$

Figure 6.18 compares the focal spot of lenses using design A and B. The lenses in Figure 6.18a were from sample 1 and had a focal length of $f = 750$ μm and a line-shaped focal spot. While the background is similar, the lens using design A shows a more pronounced focal spot compared to the lens using design B. The same is true for the lenses from sample 2 with a focal length of $f = 5$ mm compared in Figure 6.18b.

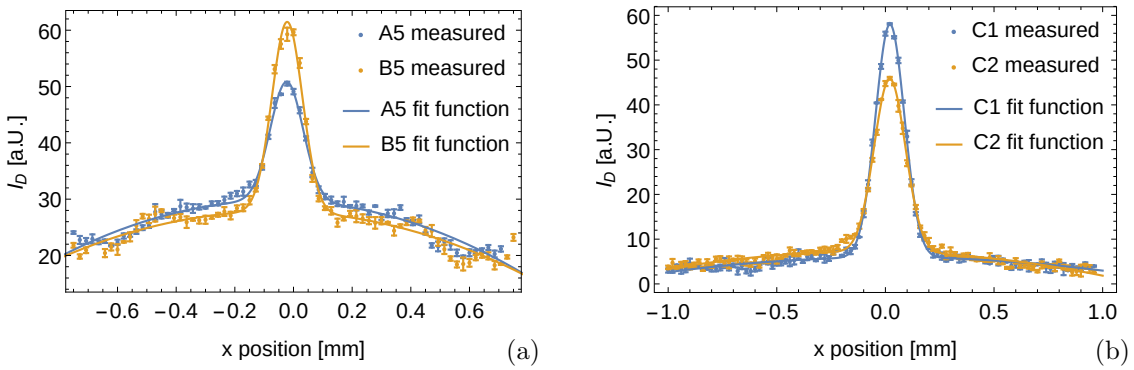

Figure 6.18: Comparison of the focal spot of lenses using the design A and B. Lenses in (a) were from sample 1 and had a focal length of $f = 750$ μm, the lenses compared in (b) are from sample 2 and have a focal length of 5 mm.

Fit parameters of all the lenses on sample 1 were collected in Table 6.3 and Table 6.4. A comparison of the parameter a in Table 6.3, indicating the height of the Gaussian, shows that all lenses built using design A show a better focusing performance, according to the scanning slit measurements.

Table 6.3: Collection of the fit parameters obtained for the Gaussians of different lenses on sample 1. The lenses had different focal length f and the detector signal in the focal plane was fitted according to Equation 6.5.

position	f [mm]	design	a [a.u.]	Δa[a.u.]	$x_0[\mu m]$	$\Delta x_0[\mu m]$	$\sigma[\mu m]$	$\Delta\sigma[\mu m]$
A1	5	A	34.8	0.5	-7	1	64	1
A2	5	B	27.1	0.5	18	1	66	1
B1	5	A	57.4	0.5	-17	1	69	1
B2	5	B	44.5	0.4	-22	1	71	1
C1	5	A	55.2	0.6	-9	1	66	1
C2	5	B	48.0	0.5	8	1	72	1
A3	0.75	A	8.1	0.5	-20	4	59	5
B3	0.75	B	9.0	0.6	-6	4	66	5
A4	0.75	B	12.5	0.6	-6	3	57	3
B4	0.75	A	13.1	0.6	-13	3	57	3
A5	0.75	B	22.4	0.9	-16	2	55	3
B5	0.75	A	37.5	1.0	-11	2	47	2

A general trend, which can be observed from the values in Table 6.3, was the superior focusing quality of lenses with a focal length of $f = 5$ mm. Besides the larger area of those lenses, the lower numerical aperture is believed to make the difference. Lenses with a focal length of $f = 750$ μm have a larger numerical aperture and show under-sampling in the outer area, causing unwanted scattering and thereby inferior focusing properties. The lenses with quadratic geometry in Table 6.3 also have a larger parameter a, compared to circular ones. This observation can be attributed to the different lens area.

When comparing the width of the focal spots, it was observed that σ is generally larger for lenses with a focal length of 5 mm. This was caused by the insufficient collimation of the incident light in the basic measurement set-up. For a focal length of 750 μm, the comparison with the simulation results in Figure 6.15 showed that the measured spot-width was limited by the slit width of 125 μm. For a larger focal length of the sub-wavelength grating lens, geometrical optics considerations predict a larger image of the thermal IR source. Consequently, larger values of σ were obtained from the scanning slit measurement.

Table 6.4 allows for comparison of the parameters obtained, when fitting the background with a quadratic function. Lenses with a focal length of $f = 750$ μm, that were measured without the 8-12 μm bandpass filter, clearly show a larger constant background indicated by the parameter b_3. This means that outside of the 8-12 μm range, the focusing performance of the lenses is rather poor.

Table 6.4: Parameters obtained when fitting the background signal with a quadratic function according to Equation 6.5. Lenses of sample 1 with a focal length of $f = 750$ μm were without the 8-12 μm bandpass filter and therefore show a larger constant background b_3.

position	b_1 $\left[\frac{a.u.}{\mu m^2}\right]$	Δb_1 $\left[\frac{a.u.}{\mu m^2}\right]$	b_2 $\left[\frac{a.u.}{\mu m}\right]$	Δb_2 $\left[\frac{a.u.}{\mu m}\right]$	b_3 [a.u.]	Δb_3 [a.u.]
A1	-1.0×10^{-6}	3×10^{-7}	-8×10^{-4}	2×10^{-4}	3.4	0.2
A2	-4×10^{-7}	3×10^{-7}	-1.3×10^{-3}	2×10^{-4}	4.0	0.2
B1	-2.6×10^{-6}	4×10^{-7}	-6×10^{-4}	2×10^{-4}	4.9	0.2
B2	-1.6×10^{-6}	3×10^{-7}	-1.6×10^{-3}	1×10^{-4}	4.1	0.1
C1	-3.4×10^{-6}	5×10^{-7}	-1.3×10^{-3}	2×10^{-4}	5.8	0.2
C2	-3.6×10^{-6}	4×10^{-7}	-1.7×10^{-3}	2×10^{-4}	6.3	0.2
A3	6.0×10^{-6}	7×10^{-7}	-6×10^{-4}	2×10^{-4}	14.6	0.2
B3	5.6×10^{-6}	9×10^{-7}	-1.2×10^{-3}	3×10^{-4}	14.9	0.3
A4	-1.7×10^{-5}	1×10^{-6}	2×10^{-4}	3×10^{-4}	27.4	0.2
B4	-1.3×10^{-5}	1×10^{-6}	-3.3×10^{-3}	3×10^{-4}	24.3	0.3
A5	-1.7×10^{-5}	1×10^{-6}	-2.3×10^{-3}	4×10^{-4}	29.6	0.3
B5	-1.7×10^{-5}	1×10^{-6}	-2.3×10^{-3}	5×10^{-4}	28.0	0.4

6.3.6 Influence of the cylinder height

To investigate the influence of the etch depth, the lenses on position C1 and B5 were remeasured for the three samples, taking the average of 3 measurements per point. Figure 6.19 shows the data from the scanning slit measurement, fitted with the function from Equation 6.5. The fit parameters obtained for the Gaussians are listed in Table 6.2.

From Figure 6.19 and the comparison of the peak height a it was found that for sample 1 with an etch depth of approximately 6.3 μm the lenses show the best focusing performance. When designing the sub-wavelength grating lenses a cylinder height of $h = 6.25$ μm was used, which is close to the etch depth for sample 1.

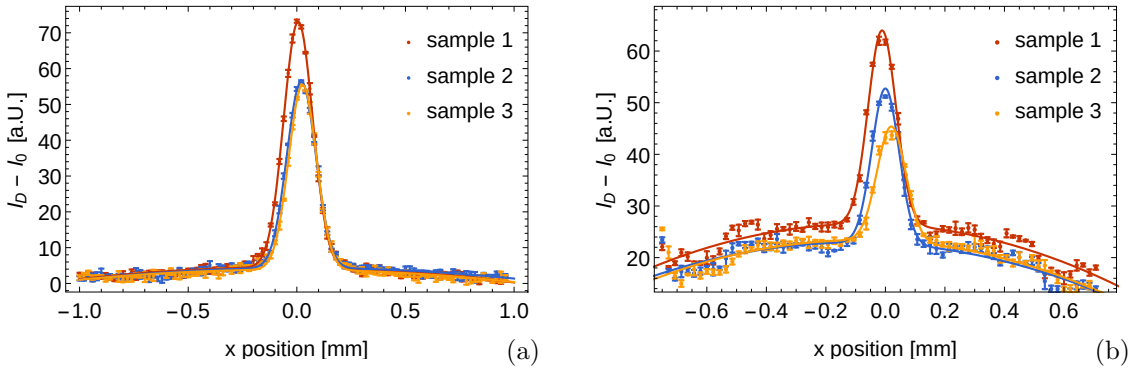

Figure 6.19: Influence of the cylinder height on the quality of the focal spot. Lenses on position C1 (a) and B5 (b) were measured for samples with different etch depth.

Table 6.5: Fit Parameters of the Gaussians in the focal plane for lenses from samples with different etch depth. The cylinder height h has an error of $\Delta h = 0.1$ μm. Comparison of the peak height a shows that the focusing performance is best for the lenses of sample 1.

position	$h[\mu m]$	sample	a[a.u.]	Δa[a.u.]	$x_0[\mu m]$	$\Delta x_0[\mu m]$	$\sigma[\mu m]$	$\Delta\sigma[\mu m]$
C1	6.3	1	68.5	0.4	6	1	66	1
C1	6.1	2	52.0	0.4	20	1	66	1
C1	6.5	3	51.5	0.4	26	1	64	1
B5	6.3	1	37.5	1.0	-11	2	47	2
B5	6.1	2	30.0	1.0	0	2	45	2
B5	6.5	3	22.2	1.1	20	3	48	3

6.3.7 Estimation of the focusing efficiency

For the estimation of the focusing efficiency the wafer with the sample lenses was removed from the set-up and measurements were taken without a lens in the optical path. The diameter of the iris aperture was adjusted to the respective value used for the measurement of the lenses on position C1 and B5 of sample 1. The 8-12 μm filter was in the optical path for all measurements and an average over 3 measurements per point was taken without any lens in the path and for the lens on position C1. An average over 8 measurements was used for the lens on position B5. Figure 6.20 shows the results of the measurements and the respective fit functions using to Equation 6.5.

The focusing efficiency was estimated by the ratio of the integrals over the fit functions and calculated to be

$$\frac{\int_{-2\sigma}^{2\sigma} I_D(x, C1) - I_0 \, \mathrm{d}x}{\int_{-1mm}^{1mm} I_D(x, \text{no lens}) - I_0 \, \mathrm{d}x} \approx 19\%$$

for the lens on position C1 and

$$\frac{\int_{-2\sigma}^{2\sigma} I_D(x, C1) - I_0 \, \mathrm{d}x}{\int_{-0.75mm}^{0.75mm} I_D(x, \text{no lens}) - I_0 \, \mathrm{d}x} \approx 4\%$$

for the lens on position C2. The respective values for σ can be found in Table 6.2. The observed large difference of the focusing efficiency, estimated from the scanning slit measurement, can again be explained by under-sampling. The lens with a focal length of 5 mm and a side length of 2 mm has a lower numerical aperture than the lens with a focal length of 750 μm and a side-length of 1.5 mm. For a large numerical aperture, the grating pitch and the distance between 2π phase jumps is similar, which causes under-sampling observed in the microscope pictures shown above. Consequently the reshaping of the wavefront by the lens is disturbed, resulting in lower focusing efficiency.

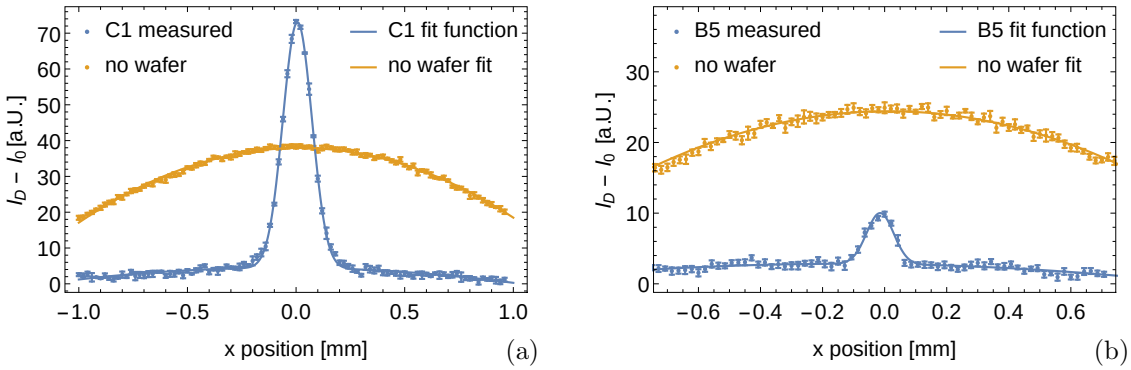

Figure 6.20: Estimation of the focusing efficiency for two sub-wavelength grating lenses on sample 1. The diameter of the iris aperture was 2.5 mm for the measurement of the lens on position C1 (a) and 2 mm for the lens on position B5 (b).

6.3.8 Comparison with a conventional Fresnel Zone Plate

Scanning slit measurements were also done for a Fresnel zone plate with a diameter of 1 mm and a focal length of 720 μm, corresponding to the one simulated in Section 5.4. Because of the low SNR, the 8-12 μm filter was not used and an average of 10 measurements was taken for each point. Furthermore an additional aperture was placed around the zone plate. The measurement data had a resolution of 101 $\times$ 11 pixels and quadratic interpolation was used for the plot in Figure 6.21.

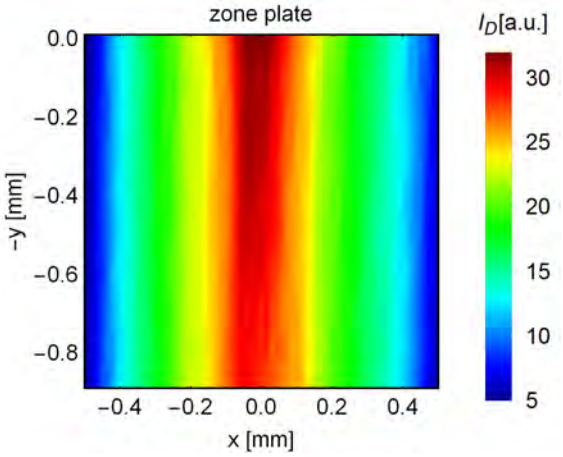

Figure 6.21: Focal spot for a zone plate with a diameter of 1 mm measured with the scanning slit method. The smoothened data had a resolution of 101×11 pixels and an average of 10 measurements was taken for each point without an additional filter to improve the SNR.

Focal spot and background were fit using Equation 6.5, giving a value of $a = (7.8 \pm 0.3)$ a.u. for the peak height and $\sigma = (80 \pm 4)$ μm for the width. Compared to the values obtained for the sub-wavelength grating lenses in Table 6.3, the height of the focal spot is similar as for lens on position A3. The width on the other hand is larger than the widths observed for the sub-wavelength grating lenses. However, in order to make a more reliable comparison it would be necessary to improve the measurement set-up, so a feasible SNR could also be achieved while using the bandpass filter to restrict the wavelength range to 8-12 μm.

7 CONCLUSION

Wafer-level infrared lenses made of dielectric gratings were investigated using numerical simulations. The sub-wavelength gratings were designed for a wavelength of 4 μm and 10 μm using a finite difference time domain program (Lumerical). In Section 4 several designs using cylindrical silicon pillars were presented. It was found that by varying the diameter of the grating pillars, the transmitted phase can be varied from 0 to 2π. This allowed for the design of a thin flat lens, but also different designs, e.g. axicons or vortex lenses, could be imagined. Investigations of the behavior for off-axis incidence showed that the grating structures also support undesired lateral modes. The onset of scattering into higher diffraction orders was accurately described by Fraunhofer far field diffraction theory, even tough the grating had a sub-wavelength structure.

Despite the possible sources of defocussing, the sub-wavelength grating lenses could be optimized for imaging with a 120° field of view, by applying an empirical correction to the formula for the lens phase. The results for a simple imaging device for a wavelength of 4 μm in Section 5 are the main findings of this work and were also presented at the SPIE Optics + Photonics conference [1]. Wave-optics simulations with a finite element program (Comsol) showed the desired sin(incidence angle) dependence for the displacement of the peak in the focal plane. The behavior of chromatic aberrations was also found to match theoretical predictions and using a Gaussian apodization function instead of a simple aperture significantly reduced the side peaks of the focal spots. In addition, a sensitivity analysis of the lens performance with respect to deviations from the ideal geometry was done to show the feasibility of production.

Lenses and simple imaging devices were also designed for a wavelength of 10 μm. An initial design, using an effective medium theory for the refractive index, presented in Section 3, had a maximum aspect ratio 1:11. By using a sub-wavelength grating design, the maximum aspect ratio could be reduced to a value below 1:5, which simplified production. The focusing behavior in the atmospheric window from 8-12 μm was also compared to a conventional Fresnel zone plate.

Test samples of lenses for a wavelength of 10 μm were produced using UV lithography and deep reactive ion etching. To be able to characterize sample lenses, a knife-edge based measurement set-up was devised and simulated with ray-tracing (APEX). However, an admissible signal to noise ratio could not be obtained with the equipment at hand and therefore a scanning slit measurement set-up was used as a back-up solution to characterize the samples. The set-up used a broadband thermal IR source and a 8-12 μm bandpass filter, results in Section 6 compare lenses with different focal length and design. For all the sample lenses a distinct focal spot could be observed, providing a proof of the lens concept for wafer-level IR optics.

Simulation and measurement results were compared, showing good agreement for the width of the focal spot. However, the simulations therefore had to be modified to account for the limited resolution of the measurement, due to the finite width of the slit. Generally it was found that lenses with a low numerical aperture show better focusing efficiency than high NA lenses. This was attributed to under-sampling of the phase profile by the grating pitch near the lens boundary. For a more detailed investigations of the IR lenses it would be necessary to upgrade the measurement set-up and increase the signal to noise ratio. Further samples also should be produced with an aperture placed directly on the wafer for better comparability of the measurements.

References

[1] L. Elsinger, P. Hadley, R. M. A. S., "Optimizing a sub-wavelength grating lens for large incidence angles," *Proc. of SPIE* **9556**, 95560O1–4 (August 2015).

[2] Voelkel, R., "Wafer-scale micro-optics fabrication," *Adv. Opt. Techn.* **1**, 135–150 (2012).

[3] Iizuka, K., [*Engineering Optics*], Springer, New York (2008).

[4] Vo, S., Fattal, D., Sorin, W. V., Peng, Z., Tran, T., Fiorentino, M., and Beausoleil, R. G., "Sub-wavelength grating lens with a twist," *IEEE Photonics Technology Letters* **26**(13), 1375–1378 (2014).

[5] A. Arbabi, Y. Horie, A. B. M. B. and Faraon, A., "Subwavelength-thick lenses with high numerical apertures and large efficiency based on high-contrast transmitarrays," *Nature Communications* **6**, 7069 (2015).

[6] F. Aieta, P. Genevet, M. K. N. Y. R. B. Z. G. and Carpasso, F., "Aberration-free ultrathin flat lenses and axicons at telecom wavelengths based on plasmonic metasurfaces," *Nano Letters* **12**(9), 4932–4936 (2012).

[7] Turunen, J. and Wyrowski, F., [*Diffractive Optics*], Akademie Verlag, Berlin (August 1997).

[8] W. Stork, N.Streibl, H. H. and P.Kipfer, "Artificial distributed-index media fabricated by zero-order gratings," *Optics Letters* **16**(24), 1921–1923 (1991).

[9] Rytov, S. M., "Electromagnetic properties of a finely stratified medium," *Soviet Physics JETP* **2**(3), 466–475 (1956).

[10] Chang-Hasnain, C. J. and Yang, W., "High-contrast gratings for integrated optoelectronics," *Adv. Opt. Photon.* **4**(3), 379–440 (2012).

[11] Klemm, A. B., Stellinga, D., Martins, E. R., Lewis, L., O'Faolain, L., and Krauss, T. F., "Focusing with planar microlenses made of two-dimensionally varying high contrast gratings," *Optical Engineering* **53**(9), 095104 1–6 (2014).

[12] Born, M. and Wolf, E., [*Principles of Optics*], Cambridge University Press, Cambridge (August 2001).

[13] Bräuer, R. and Bryngdahl, O., "Design of antireflection gratings with approximate and rigorous methods," *Applied Optics* **33**(34), 7875–7882 (1994).

[14] John D. Joannopoulos, Steven G. Johnson, J. N. W. and Meade, R. D., [*Photonic Crystals - Molding the Flow of Light (Second Edition)*], Princton University Press, New Jersey (2008).

[15] Weber, M. J., [*Handbook of optical materials*], CRC Press, Boca Raton (2003).

[16] Polycarpou, A. C., [*Introduction to the Finite Element Method in Electromagnetics*], Morgan Claypool (2006).

[17] Vadim Karagodsky, F. G. S. and Chang-Hasnain, C. J., "Theoretical analysis of subwavelength high contrast grating reflectors," *Optics Express* **18**(16), 16973–16988 (2010).

[18] Yee, K. S., "Numerical solution of initial boundry value problems involving maxwell's equations in isotropic media," *IEEE Transactions on Antennas and Propagation* **141**(3), 302–307 (1966).

[19] Gedney, S. D., [*Introduction to the Finite-Difference Time-Domain (FDTD) Method for Electromagneitcs*], Morgan Claypool (2011).

[20] Bérenger, J.-P., [*Perfectly Matched Layer (PML) for Computational Electromagnetics*], Morgan Claypool (2007).

[21] André Nicolet, Sébastien Guenneau, C. G. and Zolla, F., "Modelling of electromagnetic waves in periodic media with finite elements," *Journal of Computational and Applied Mathematics* **168**, 321–329 (2004).

[22] Horwitz, J. W., "Infrared refractive index of polyethylene and polyethylene-based material," *Optical Engineering* **50**(9), 093603 1–4 (2011).

[23] A. H. Firester, M. E. H. and Sheng, P., "Knife-edge scanning measurements of subwavelength focused light beams," *Applied Optics* **16**(7), 1971–1974 (1977).

[24] W. Plass, R. Maestle, K. W. A. V. and Giesen, A., "High-resolution knife-edge laser beam profiling," *Optics Communications* **134**, 21–24 (1997).

[25] Ayotte, N., *Matlab GDS Photonics Toolbox* (02 Jun 2014). `http://www.mathworks.com/matlabcentral/fileexchange/46827-nicolasayotte-matlabgdsphotonicstoolbox`.

[26] Kuo-Shen Chen, Arturo A. Ayón, X. Z. S. M. S., "Effect of process parameters on the surface morphology and mechanical performance of silicon structures after deep reactive ion etching (drie)," *Journal of Microelectromechanical Systems* **11**(3), 264–275 (2002).